



MODIFICATION OF $\text{CO}_3\text{O}_4/\text{CUBI}_2\text{O}_4$ PHOTOCATALYST FOR WASTEWATER
TREATMENT



PUNYANUCH THAMMAACHEEP

A Thesis Submitted to the Graduate School of Naresuan University
in Partial Fulfillment of the Requirements
for the Master of Science in Chemistry (Type A 2)

2022

Copyright by Naresuan University

MODIFICATION OF $\text{CO}_3\text{O}_4/\text{CuBi}_2\text{O}_4$ PHOTOCATALYST FOR WASTEWATER
TREATMENT



PUNYANUCH THAMMAACHEEP

A Thesis Submitted to the Graduate School of Naresuan University
in Partial Fulfillment of the Requirements
for the Master of Science in Chemistry (Type A 2)

2022

Copyright by Naresuan University

Thesis entitled "Modification of $\text{Co}_3\text{O}_4/\text{CuBi}_2\text{O}_4$ photocatalyst for wastewater treatment"

By PUNYANUCH THAMMAACHEEP

has been approved by the Graduate School as partial fulfillment of the requirements for the Master of Science in Chemistry (Type A 2) of Naresuan University

Oral Defense Committee

..... Chair
(Assistant Professor Hathaithip Sintuya, Ph.D.)

..... Advisor
(Associate Professor Duangdao Channei, Ph.D.)

..... Co Advisor
(Assistant Professor Panatda Jannoey, Ph.D.)

..... Co Advisor
(Kantapat Chansaenpak, Ph.D.)

..... Internal Examiner
(Assistant Professor Wikorn Punyain, Ph.D.)

Approved

.....
(Associate Professor Krongkarn Chootip, Ph.D.)

Dean of the Graduate School

Title	MODIFICATION OF $\text{Co}_3\text{O}_4/\text{CuBi}_2\text{O}_4$ PHOTOCATALYST FOR WASTEWATER TREATMENT
Author	PUNYANUCH THAMMAACHEEP
Advisor	Associate Professor Duangdao Channei, Ph.D.
Co-Advisor	Assistant Professor Panatda Jannoey, Ph.D. Kantapat Chansaenpak, Ph.D.
Academic Paper	M.S. Thesis in Chemistry (Type A 2), Naresuan University, 2022
Keywords	cobalt oxide, copper bismuth oxide, composite materials, photocatalysis

ABSTRACT

Heterogeneous photocatalysis is an effective technology for the removal of organic dyes in textile wastewater. Metal oxide semiconductors have been extensively applied as photocatalysts in the last few decades. Herein, we report the synthesis of cobalt oxide (Co_3O_4), copper bismuth oxide (CuBi_2O_4) and $\text{Co}_3\text{O}_4/\text{CuBi}_2\text{O}_4$ composite powders by a co-precipitation method. The effect of Co_3O_4 addition on phase composition and microstructure of CuBi_2O_4 is studied using XRD, TEM and SEM. The surface area and pore structure of composite samples at different amounts of Co_3O_4 addition has been studied by nitrogen adsorption-desorption isotherm based on BET theory. Optical properties of the prepared photocatalyst are also investigated by DRS UV-Vis measurements. The intensity of photoluminescence (PL) is also used to measure of the electron hole recombination in the unmodified photocatalyst compared with the composite samples.

The photocatalytic activity of the prepared samples is evaluated under visible light with presence of methylene blue (MB) as target pollutant. Results show that coupling Co_3O_4 with CuBi_2O_4 could effectively promote photogenerated electron transfer in heterojunction, which is able to retard recombination process and thus improve their photocatalytic performance. In this system, 50 wt% $\text{Co}_3\text{O}_4/\text{CuBi}_2\text{O}_4$ exhibit the best photocatalytic activity in degrading 28% of MB within 120 min under visible irradiation.

Hence, the formation of a heterojunction between two photocatalysts is an efficient way to degrade the environmental pollutants in wastewater with the usage of photon energy, that can be further adapted for use in practical application.



ACKNOWLEDGEMENTS

This research was financially supported by Thailand Graduate Institute of Science and Technology, TGIST (Grant no. SCA-CO-2563-12179-TH/2563).

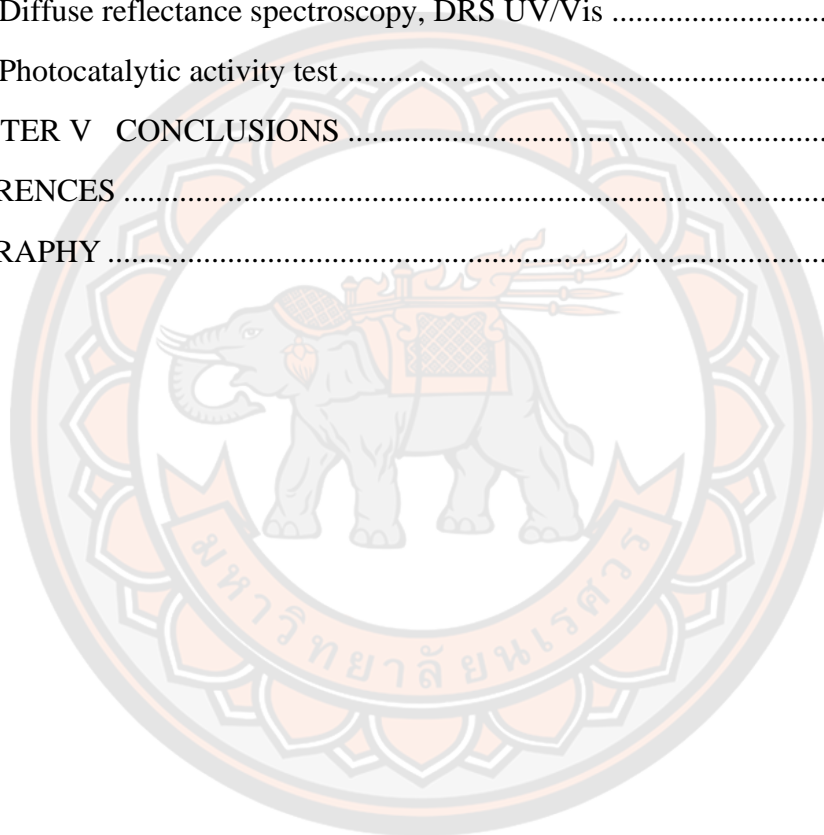
PUNYANUCH THAMMAACHEEP



TABLE OF CONTENTS

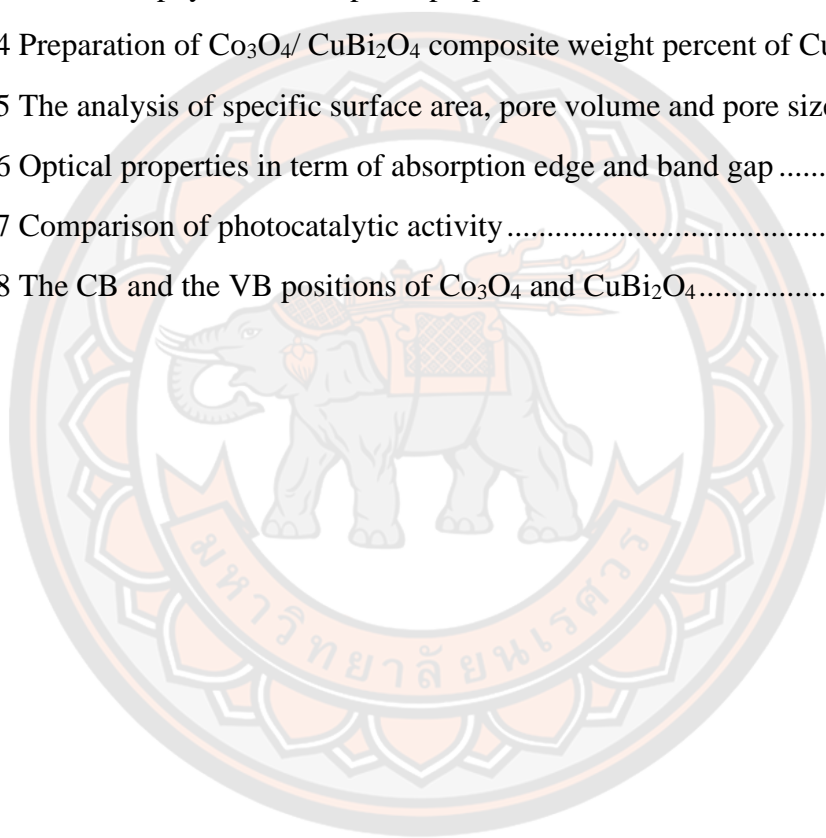
	Page
ABSTRACT.....	C
ACKNOWLEDGEMENTS.....	E
TABLE OF CONTENTS.....	F
LIST OF TABLE.....	H
LIST OF FIGURE.....	I
CHAPTER I INTRODUCTION.....	1
1.1 General Background.....	1
1.2 The objective of study.....	6
1.3 Scope and limitation of study.....	7
1.4 The Benefits of study.....	7
CHAPTER II LITERATURE REVIEW.....	8
2.1 Synthetic dye.....	8
2.2 Advance Oxidation processes (AOPs).....	9
2.3 Photocatalysis.....	10
2.4 Recombination process.....	11
2.5 Modification of photocatalyst.....	12
2.6 Cobalt oxide (Co ₃ O ₄).....	14
2.7 Copper bismuth oxide (CuBi ₂ O ₄).....	16
2.8 Literature Review and articles research.....	17
CHAPTER III RESEARCH METHODOLOGY.....	27
3.1 Chemicals and reagents.....	27
3.2 Synthesis of photocatalyst.....	27
3.3 Material characterizations.....	30
3.4 Photocatalytic degradation.....	31
CHAPTER IV RESULTS AND DISCUSSION.....	33

4.1 X-ray diffraction technique (XRD)	33
4.2 The Brunauer–Emmett–Teller, BET.....	35
4.3 Transmission electron microscope technique, TEM	37
4.4 Scanning electron microscope technique, SEM	38
4.5 Photoluminescence spectroscopy (PL).....	39
4.6 Diffuse reflectance spectroscopy, DRS UV/Vis	40
4.7 Photocatalytic activity test.....	43
CHAPTER V CONCLUSIONS	49
REFERENCES	50
BIOGRAPHY	61



LIST OF TABLE

	Page
Table 1 Photocatalyst energy level gap and the boundaries of the valence band (E_{VB}) and conduction band (E_{CB}) positions	2
Table 2 Chemical, physical, and optical properties of Co_3O_4	15
Table 3 Chemical, physical, and optical properties of $CuBi_2O_4$	17
Table 4 Preparation of $Co_3O_4/ CuBi_2O_4$ composite weight percent of $CuBi_2O_4$	29
Table 5 The analysis of specific surface area, pore volume and pore size	36
Table 6 Optical properties in term of absorption edge and band gap	43
Table 7 Comparison of photocatalytic activity	44
Table 8 The CB and the VB positions of Co_3O_4 and $CuBi_2O_4$	46



LIST OF FIGURE

	Page
Figure 1 Photocatalyst and energy level gap, showing the difference in energy levels of the valence band and conduction band (7)	3
Figure 2 Photocatalytic mechanism (8)	4
Figure 3 Type-II heterojunction staggered (14).....	6
Figure 4 Proposed mechanism of the oxidation of benzene by hydroxyl radicals (24)	10
Figure 5 Simple schematic of photocatalytic process (25).....	11
Figure 6 electron/hole recombination (28)	12
Figure 7 n-and p-type doping in a semiconductor (30).....	13
Figure 8 Different types of semiconductor heterojunctions (31,32).....	13
Figure 9 Cubic Co_3O_4 spinel structure (35)	14
Figure 10 Tetragonal structure of CuBi_2O_4 (36,37)	16
Figure 11 Absorption spectral changes with photocatalytic degradation time of SA dye (38).....	18
Figure 12 Degradation mechanism MB and CV by rGO-TiO ₂ /Co ₃ O ₄ nanocomposite (39).....	19
Figure 13 Graph plot of C/C ₀ Vs time of photocatalyst in MB solution (40).....	20
Figure 14 (a) UV-vis spectral change of MB dye after addition of $\text{MnFe}_2\text{O}_4\text{-Co}_3\text{O}_4$ (b) The plot of C/C ₀ and 1-(C/C ₀) versus time after addition of $\text{MnFe}_2\text{O}_4\text{-Co}_3\text{O}_4$ (41)	21
Figure 15 SEM images of the samples prepared at 120 °C for 6 h (A), 12 h (B, D, E, F) and (G) Effects of CuBi_2O_4 on the photocatalytic oxidation of MB under 500-W xenon lamp irradiation	22
Figure 16 Proposed photocatalytic degradation mechanism and the energy level alignment (43).....	23
Figure 17 Photocatalytic degradation of DR16 over different photocatalysts (44).....	24
Figure 18 Schematic of photocatalytic reaction over the ZnO/CuBi ₂ O ₄ /PS system (45)	25

Figure 19 Preparation of Co_3O_4 via co-precipitation method.....	28
Figure 20 Preparation of CuBi_2O_4 via co-precipitation method.....	29
Figure 21 Preparation of $\text{Co}_3\text{O}_4/\text{CuBi}_2\text{O}_4$ composites	30
Figure 22 Photocatalytic degradation of $\text{Co}_3\text{O}_4/\text{CuBi}_2\text{O}_4$ composites.....	31
Figure 23 Calibration curve of methylene blue with different concentrations.....	32
Figure 24 XRD pattern of Co_3O_4	33
Figure 25 XRD pattern of tetragonal structure CuBi_2O_4	34
Figure 26 The XRD patten of $\text{Co}_3\text{O}_4/\text{CuBi}_2\text{O}_4$ composites	35
Figure 27 The nitrogen adsorption-desorption isotherm of the as-synthesized photocatalyst	37
Figure 28 TEM images of (a) Co_3O_4 , (b) CuBi_2O_4 , (c) 20%, (d) 50%, and (e) 80% wt. $\text{Co}_3\text{O}_4/\text{CuBi}_2\text{O}_4$	38
Figure 29 SEM images of (a) Co_3O_4 , (b) CuBi_2O_4 , (c) 20%, (d) 50% and.....	39
Figure 30 PL spectra of pure Co_3O_4 , pure CuBi_2O_4 and $\text{Co}_3\text{O}_4/\text{CuBi}_2\text{O}_4$ composites	40
Figure 31 Charge separation through a type-II heterojunction of $\text{Co}_3\text{O}_4/\text{CuBi}_2\text{O}_4$ composites.....	40
Figure 32 (a) UV–vis diffuse reflectance spectra (b) Kubelka–Munk absorbance spectra, and (c) band gap estimation according to Tauc's model.....	42
Figure 33 Photocatalytic degradation of MB over different photocatalysts in visible light	44
Figure 34 The apparent reaction rate constants	45
Figure 35 Schematic of photocatalytic reaction over the $\text{Co}_3\text{O}_4/\text{CuBi}_2\text{O}_4$ composite .	47
Figure 36 Fluorescence spectra of TAOH solutions generated by $\text{Co}_3\text{O}_4/\text{CuBi}_2\text{O}_4$ composite	48

CHAPTER I

INTRODUCTION

1.1 General Background

The problem of water pollution stems from the industrial wastewater due to the rapid expansion of the textile and garment industry have been built. In 2020, there were 4,823 factories in the textile and garment industry (1), leading to rapid developments in both production processes and exports. Water is the latter used in all processes such as fiber manufacturing, spinning, weaving, knitting, bleaching and dyeing.

Most of the dye molecules are composed of highly stable aromatic rings lead to a higher level of biodegradation. As a result, the contaminated water is transformed into what we call wastewater, whereby there is a rise in temperature, an odor, a color, and termination of life due to the high amount of organic matter in the water. The lack of oxygen and the effect of wastewater is also an inhibitor of various microorganisms. It is pertinent that the industrial plant be used in practice to improve the quality of wastewater to meet the effluent standards set before it is released into the environment.

There are some wastewater treatment techniques that have been used in textile dyeing plants in Thailand including (2);

- Chemical coagulation–flocculation: it is a method for separating smaller suspended solids from wastewater by using chemicals to precipitate, such as alum and lime, etc.(3)

- Ozone oxidation process (O_3); this method is an oxidizing agent with a high ability to decompose organic matter. It is commonly used in color degradation and organic substances in the wastewater treatment of the dyeing industry. (4)

- Electrochemical processes; it is a redox reaction which shows the relationship between chemistry and electrical energy. Electrochemical reduction reactions mostly are applied to effluents discoloration in dyeing (5).

- Adsorption; it is a process whereby porous adsorbent such as activated carbon is used to adsorb pollutant that cannot be eliminated in chemical precipitation systems or biological treatment systems. It is often used as a final system before

draining the wastewater from the factory. However, adsorption process cannot efficiently break the chemical bond of dye and other pollutant molecules. (6)

Advanced Oxidation Processes (AOPs) are efficient methods for treating wastewater that generally use the ultimate oxidant, photon energy and photocatalyst for the remediation of contaminants in wastewater. The mechanism of AOPs in oxidizing organic compounds in water can be classified into 2 types especially based on the ability of electrons and holes during redox reactions, including (i) single-phase systems and (ii) two-phase system (7).

The most used metal oxide semiconductor as a photocatalyst is shown in **Table 1** and **Figure 1.**, respectively. The photocatalyst with different band gap requires the difference in photon energy to irradiate electron-hole pairs for photocatalytic reaction.

Table 1 Photocatalyst energy level gap and the boundaries of the valence band (E_{VB}) and conduction band (E_{CB}) positions

Photocatalyst	Band gap (eV)	E_{CB} (eV)	E_{VB} (eV)
Fe_2O_3	2.00–2.20	0.30–0.60	2.40–2.70
TiO_2 (rutile)	3.00–3.70	–0.05–0.15	2.92–2.95
TiO_2 (anatase)	3.20	–0.10	3.10
WO_3	2.60–2.80	0.24,0.40,0.73	2.99,3.20,3.45
$BiVO_4$	2.40	0.46	2.86
ZnO	3.20,3.30	–0.25,0.20	2.95,3.10
MoS_2	1.73	–0.04	1.69
CuO	1.55	–.051	1.04
Cu_2O	2.00	–0.70	1.30
$CuBi_2O_4$	1.50	–0.44	0.94
Co_3O_4	1.37	0.17	1.54
CeO_2	3.00	-0.44	2.56

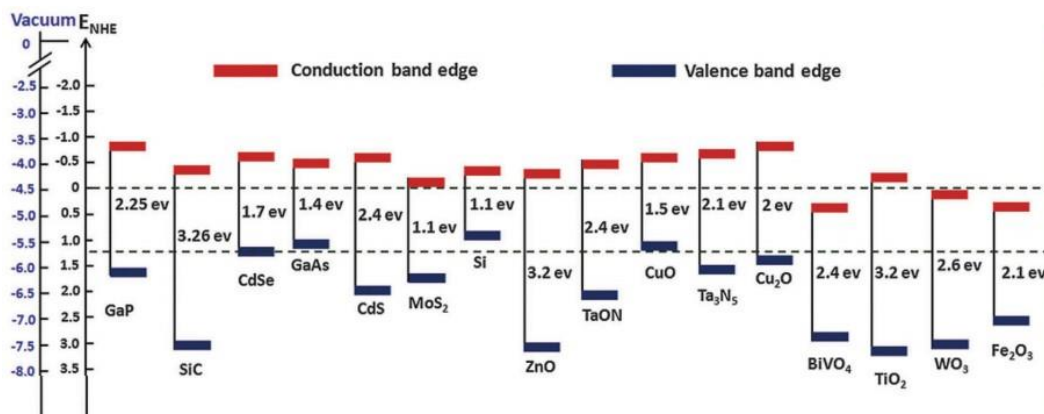


Figure 1 Photocatalyst and energy level gap, showing the difference in energy levels of the valence band and conduction band (7)

However, the photocatalytic activity of semiconductor in heterogenous system is limited by its easy recombination of the formed electrons and holes, therefore inhibiting the application under light irradiation. Suppressed electron-hole recombination is the challenge for photocatalysis research fields. Usually, the recombination rate of electron and hole increases linearly. If the reduction reaction can occur quickly, this means that the conduction band contains more electrons of the semiconductor. This results in a decrease in the rate of recombination of electrons and holes and the efficiency of the oxidation reaction could lead to a tremendous increase in efficiency to decompose organic matter on the surface of the catalyst photocatalytic mechanism or photocatalysis reaction mechanism, as shown in **Figure 2 (8)**

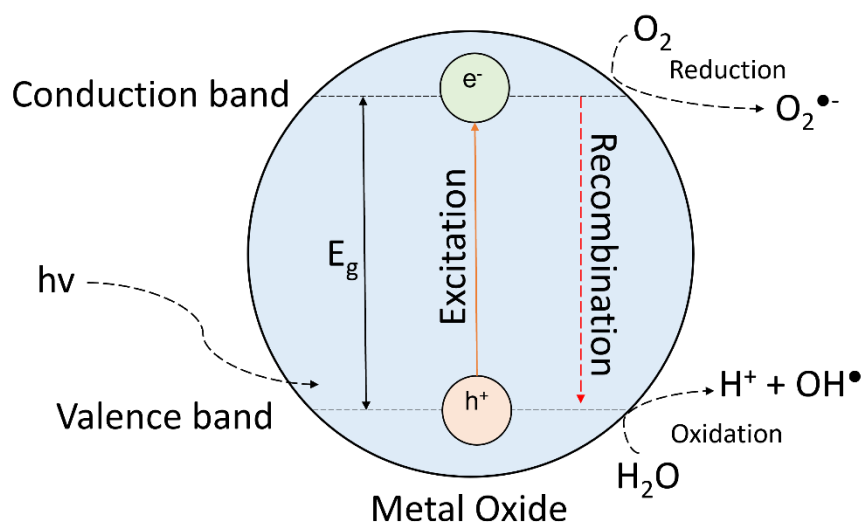


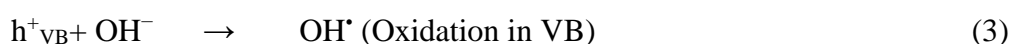
Figure 2 Photocatalytic mechanism (8)

The photocatalytic mechanism in water of heterogeneous photocatalyst is initiated by the absorption of light transmitted through water to the catalyst whose photon energy ($h\nu$) is greater than or equal to the band energy.

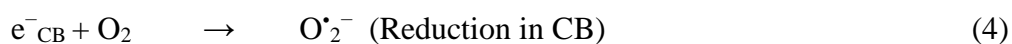
Electrons are excited from the valence band to move towards the conduction band, as shown in Equation 1

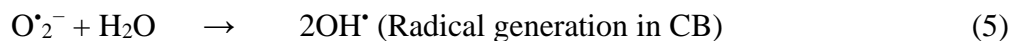


For oxidation reaction in the valence band with holes, the hole reacts with water and hydroxide ions (OH^-) to form a hydroxyl radical ($\text{OH}\cdot$) as written in Equations 2 and 3, respectively. The produced hydroxyl radical ($\text{OH}\cdot$) being a very strong oxidant in the photocatalytic process can decompose various organic substances.



In the meantime, the electrons in the conduction band reacts with the dissolved oxygen for the reduction reaction, forms a superoxide radical ($\text{O}_2^{\cdot-}$), which is a reducing agent and a free radical that can degrade organic compounds. Hydroxyl radicals can also be involved in the reaction of further active superoxide radical and H_2O molecule, as shown in Equations 4 and 5, respectively.





The final products of organic decomposition are carbon dioxide, water and small organic molecules produced by the redox reaction of hydroxyl radicals at the surface of the catalyst, as shown in Equation 6



In this study, we are interested in modification of cobalt oxide (Co^3O^4) photocatalyst. This material has a cubic structure with an energy band gap of approximately 1.48–2.19 eV (9), enabling it to respond to light in the visible region. It has potential for various optical applications such as optical catalysts under visible-light-driven photocatalyst(10), electrode anode in lithium battery (11), gas sensor (12) and photoelectrochemical water separation (13) etc.

Although Co^3O^4 responds well to visible light, in several research papers indicate that its catalytic efficiency is not as good as expected due to the high recombination rate of e^- and h^+ .

To enhance the photocatalytic efficiency of Co^3O^4 , making semiconductor-based composite materials is another modification method to reduce the recombination rate of e^- and h^+ . If two semiconductor materials with the matched energy level position are combined to form a type II semiconductor heterostructure, the carrier transfer between them is shown in **Figure 3** (14). Under the action of energy level difference, electrons transfer from a photocatalyst with a high conduction band level to another photocatalyst with a low conduction band level, while holes transfer from a semiconductor with a low valence band to a semiconductor with a high valence band, thus facilitating the carrier transfer in promoting greater separation of photogenerated carriers on semiconductors(14).

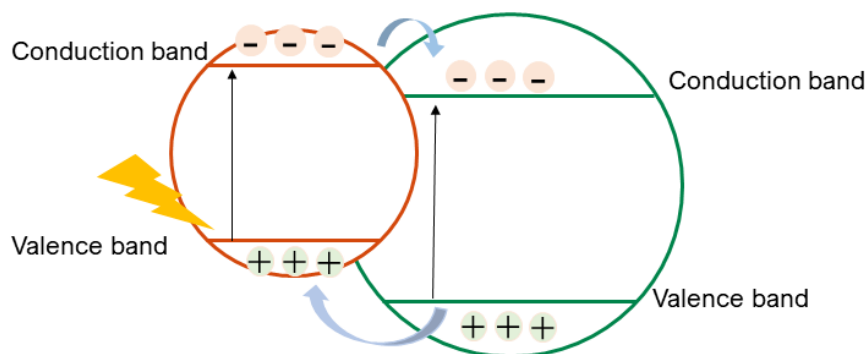


Figure 3 Type-II heterojunction staggered (14)

In the present report we have selected p-type copper bismuth oxide (CuBi_2O_4) due to the band alignment of CuBi_2O_4 is matched with Co_3O_4 to form heterojunction with matched band structure. Their energy gap of 1.50–1.80 eV corresponds to a wavelength within the visible light spectrum (15).

Therefore, this work contributes in enhancing the electron/hole pair transportation and subsequently in suppressing the recombination of electron–hole pairs in their heterostructure of Co_3O_4 by composite with CuBi_2O_4 photocatalyst to the promoted charge transport and charge separation together with light irradiation.

1.2 The objective of study

1. To synthesize pure Co_3O_4 photocatalytic material and CuBi_2O_4 by co-precipitation.
2. To synthesize composite materials, $\text{Co}_3\text{O}_4/\text{CuBi}_2\text{O}_4$ at different ratios.
3. To study the change in structural, morphological, surface morphology, and optical properties of single-phase Co_3O_4 and CuBi_2O_4 photocatalyst compared to composite materials.
4. To compare the photocatalytic ability of $\text{Co}_3\text{O}_4/\text{CuBi}_2\text{O}_4$ composites with single-phase Co_3O_4 and CuBi_2O_4 photocatalyst in the degradation of methylene blue under visible light.

1.3 Scope and limitation of study

1. Single-phase Co_3O_4 and CuBi_2O_4 , and $\text{Co}_3\text{O}_4/\text{CuBi}_2\text{O}_4$ composites at different weight ratios (% wt) were synthesized by co-precipitation method.

2. Study the change of structural, morphological, surface morphology, and optical properties of the prepared photocatalyst of composite materials $\text{Co}_3\text{O}_4/\text{CuBi}_2\text{O}_4$ compared to single-phase Co_3O_4 and CuBi_2O_4 photocatalyst via different analytical techniques in materials science including;

- i. X-ray diffraction, XRD
- ii. The adsorption/desorption of N_2 on the surface in combination with the adsorption theory of Brunauer–Emmett–Teller, BET
- iii. Transmission electron microscope, TEM
- iv. Scanning electron microscope, SEM
- v. Photoluminescence spectroscopy, PL
- vi. Diffuse reflectance spectroscopy, DRS

3. Study the photocatalytic activity of the as – prepared samples (single-phase Co_3O_4 , CuBi_2O_4 , and $\text{Co}_3\text{O}_4/\text{CuBi}_2\text{O}_4$ composites) in laboratory-scale by the photocatalytic degradation of synthetic dye wastewater (methylene blue, MB) under visible light irradiation

1.4 The Benefits of study

1. A new type of Co_3O_4 and CuBi_2O_4 composite material with better photocatalytic capability could help decompose a broad range of organic matters in the future.

2. The modification technique by the coupling of two semiconductors with the favorable energy diagram is not only used for Co_3O_4 and CuBi_2O_4 , but for a wide range of any semiconductor photocatalysts

3. Photocatalysis may be used as another method of solving the problem of water pollution.

CHAPTER II

LITERATURE REVIEW

2.1 Synthetic dye

This chapter explain the effect of dyes and pigments on water pollution. A dye is a colored substance that chemically bonds to the substrate to which it is being applied for imparting color to textile, paper, leather, plastic and other materials. In the textile manufacturing, water is extensively required at every step of textile processing operations and finishing process. Water is used not only in the washing fabric, but also for rinsing the treated fabrics, leading to large amount of chemicals and toxic materials used for wet processing released into the environment.

Most of the pigments in synthetic dyes consist of organic and inorganic compounds which the azo group is placed between aromatic rings. Typical water-soluble azo dye can generate carcinogenic benzidine and transfer of contaminant to water streams and further movement into soil. Therefore, such polluted water dyeing occurred as a result of water pollution related to chemical contamination of the aquatic environment (16).

2.1.1 Dye classification

Natural dyes are generally obtained from natural sources such as plants, minerals, fruits, flowers, leaves, roots, or bark, whereas synthetic dyes are often made from chemicals in laboratories. There are 3 types of dyes divide via the charge of structure. According to their chemical structures, dyes can be divided into three types based on ionic charge namely (i) anionic dyes, (ii) cationic dyes, and (iii) nonionic dyes.

Another classification is dependent on the chemical structures and application of these dyes on an industrial scale including acidic, basic, mordant, reactive, direct, disperse, sulfur dye, pigment, and azo insoluble (17).

2.1.2 Synthetic dyes

Synthetic dyes have been used for many purposes such as the coloring of natural fibers, in the food, leather, cosmetic or pharmaceutical industries. Thus, by the year 1900, synthetic dyes were more economical. It has become increasingly

popular and widely used in industries instead of natural dyes due to its lower costs, retain the color for longer, and much more resistant at lower pH. However, there are several disadvantages of synthetic dyes. The effluents also contain heavy metals, high chemicals, high temperature, strong acids, and heavy metal, that are toxic, carcinogenic and can cause skin and eye irritation (17). When the release of pollutants into the environment, all kinds can have negative effects on the environment as increasing in biochemical oxygen demand (BOD), affecting the pH and chemical oxygen demand (COD) (18).

Since most synthetic dyes are not biodegradable, they can react with organic matter from wastewater products to form dangerous aromatic compounds resulting in mutagenicity in aquatic life and cytotoxicity. They can also cause DNA fragmentations, allergies, skin irritations, and malfunctioning of various organs when acted upon by different biotic and abiotic factors due to the formation of toxic breakdown products. (19,20)

2.2 Advance Oxidation processes (AOPs)

Advanced oxidation processes (AOPs) employing powerful hydroxyl such as hydroxyl radicals (OH^\bullet) were first proposed in the 1980s to treat almost all organic pollutants and remove some toxic in industrial wastewater and drinking water (21).

2.2.1 Hydroxyl Radical (OH^\bullet)

Hydroxyl radical is the most reactive oxidizing agent in water treatment, with an oxidation potential between 2.8 V (pH 0) and 1.95 V (pH 14) vs. saturated calomel electrode (SCE), which is the most commonly used as reference electrode in aqueous solutions. (22)

Hydroxyl radicals are highly reactive species that attack organic pollutants through four basic pathways inducing radical addition, hydrogen abstraction, electron transfer, and radical combination (23). Their reactions with organic compounds produce carbon-centered radicals are briefly summarized in **Figure 4**. (24)

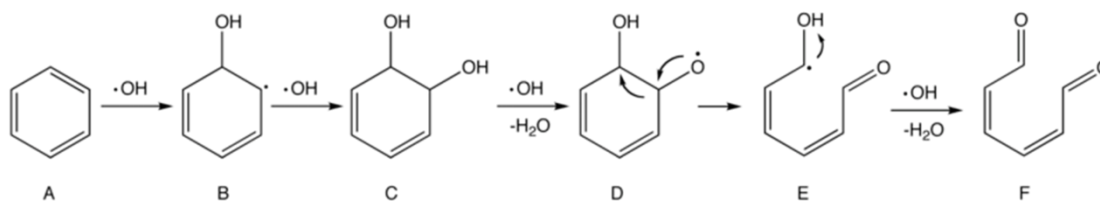


Figure 4 Proposed mechanism of the oxidation of benzene by hydroxyl radicals
(24)

2.3 Photocatalysis

Photocatalysis is a process in which light energy is used to drive pairs of chemical reactions through the absorption of photon energy by photocatalyst, in which an electron-hole pair is generated. In this regard, the use of heterogeneous photocatalysts based on nanosized metal oxides have gained great interest in the photocatalytic system due to their ability to produce charge carriers when they are irradiated by photon energy with an energy of equal to or more than their band gap. Normally, semiconductors have a band structure in which the conduction band (CB) is separated from the valence band (VB) by a band gap. After light irradiation, photogenerated electrons are excited to the CB, leaving the holes in the VB.

After that, the electron in VB gets interacted with molecular oxygen to superoxide radical anion (O_2^-) via reduction reaction. In the mean times, the valence band hole will react with adsorbed hydroxide ions (OH^-) or water on the surface to form the hydroxyl radicals (OH^\bullet). Both of superoxide radicals and hydroxyl radicals are strong oxidizing agents that can involve the photocatalytic process with the highest possible rate via redox reaction.

Oxidizing agents such as hydroxyl radicals can degrade organic compounds to carbon dioxide, water and small less toxic fragment as reaction products. Photochemical reactions occur in heterogeneous systems comprising suspended inorganic semiconductor nanoparticles or in homogeneous systems in which the molecular catalysts are solvated-metal complexes, as shown in **Figure 5**.(25)

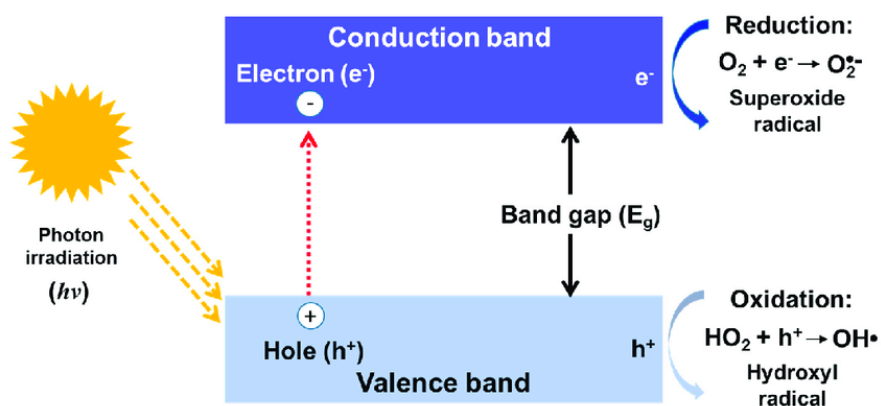


Figure 5 Simple schematic of photocatalytic process (25)

2.4 Recombination process

The electron–hole pair is the fundamental unit of carrier charge and recombination in semiconductors. Recombination process corresponds to the excited electron jumping down from the top conduction band (CB) to recombine with holes in the valence band (VB) results in the release of energy known as recombination, as shown in **Figure 6**

The strength and kind of the resulting energy is influenced by the material's typical band gap energy and the presence of imperfections within the material that can operate as charge carrier traps.

In photocatalysis, electron hole pairs are generated when catalytic semiconductor particles are illuminated with photon energy. The limitation of photocatalytic degradation is due to the recombination of electron-hole (e^-/h^+) pairs.

The unwanted recombination process must be prevented as much as possible to suppress charge recombination.

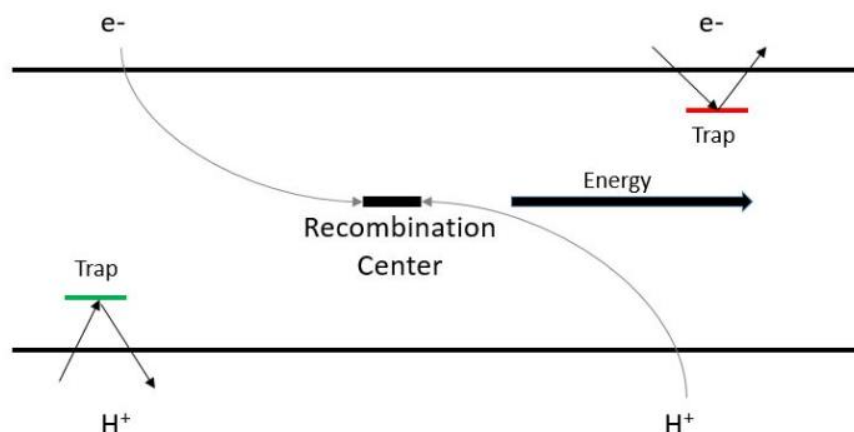


Figure 6 electron/hole recombination (28)

2.5 Modification of photocatalyst

To inhibit the electron/hole pair recombination and increase photocatalytic reaction, the way to modify photocatalyst is divided into two main methods including (i) doping with transition metals and (ii) creating heterojunction structures.

2.5.1 Metal doping

Doping of transition metal ions into semiconductors not only helps trapping excited electrons, but also modifies their optical or structural electrochemical properties. (29) In some cases, doping of some substances can change the ability of a semiconductor to conduct electricity. This is generally found for n-type doping or p-type doping, as shown in **Figure 7**

-n-type semiconductor is a semiconductor doped with a donor element and appears to be a minority carrier. In an n-type semiconductor, the Fermi level is greater than that of the intrinsic semiconductor and lies closer to the conduction band than the valence band. (30)

-p-type semiconductor is a semiconductor filled with electron acceptor element in which there are more holes than electrons. In the p-type semiconductor, the Fermi level appears to be the majority and the electrons are the minority carrier. For p-type semiconductors, the Fermi level is below the intrinsic semiconductor and lies closer to the valence band than the conduction band. (30)

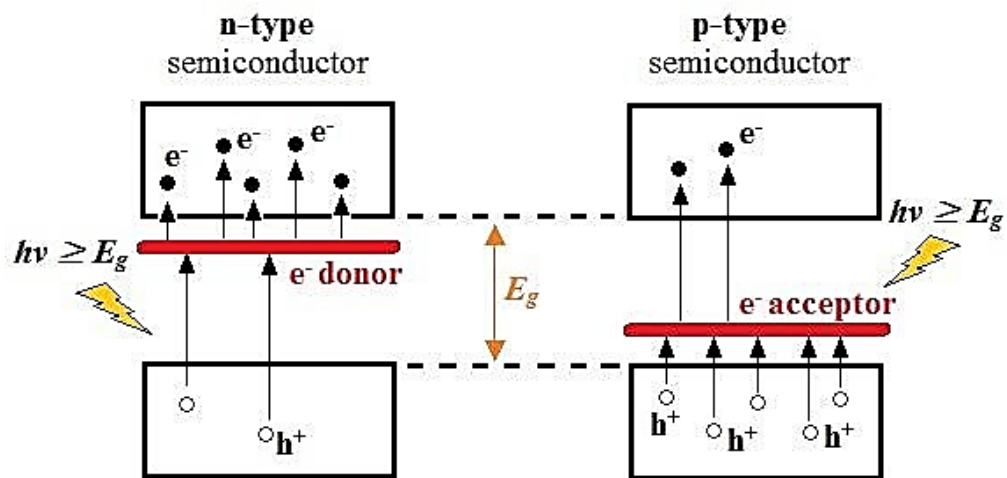


Figure 7 n-and p-type doping in a semiconductor (30)

2.5.2 Composite photocatalyst

In general, a composite photocatalyst is a material which is produced from two or more different materials two materials with different state of energy levels (VB and CB positions). In that case, the formed heterojunction composite can be classified into three different types, which are depicted in **Figure 8**

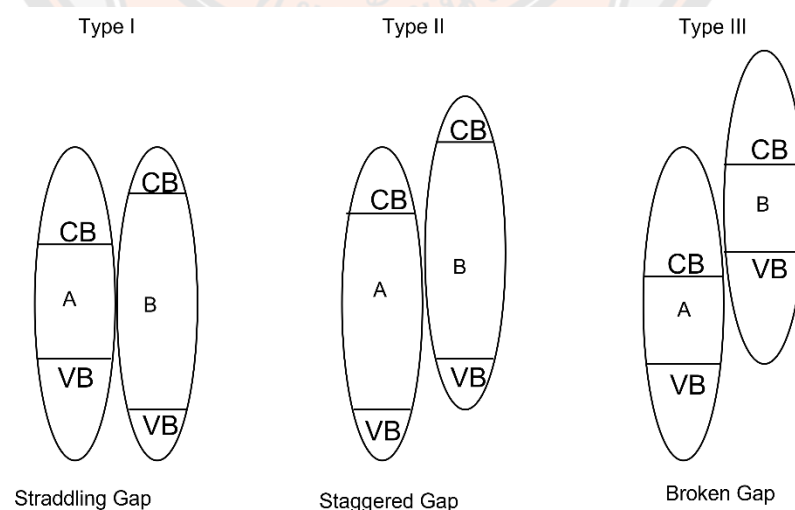


Figure 8 Different types of semiconductor heterojunctions (31,32)

- For type I heterojunction composite, the VB of semiconductor B is lower than that of semiconductor A, and the CB of semiconductor B is higher than that of semiconductor A. When the charge carriers are generated by photon with enough energy, the electrons can transfer from CB (semiconductor B) to CB (semiconductor A) and the holes can be transferred from VB (semiconductor B) to VB (semiconductor A). As a result, all charge carriers are accumulated on semiconductor A and thus charge carrier separation could not be achieved.

- For type II heterojunction composite, both the VB and CB of semiconductor B are higher than that of semiconductor A. Hence, the photo generated electron can transfer from CB (semiconductor B) to CB (semiconductor A); and the holes are simultaneously transferred from VB (semiconductor A) to VB (semiconductor B). As a result, electron and holes are separated from each other, and consequently, the reduction of charge carrier recombination is accomplished.

- For type III heterojunction composite, the transfer of charge carriers is as same as in type I. The only difference is that the band positions are even further so that the VB of semiconductor B is higher than CB of semiconductor A. This arrangement of band position is also known as broken-gap situation. However, this model has hardly been used to improve the separation of charge carriers for photocatalysis. (31,32)

2.6 Cobalt oxide (Co₃O₄)

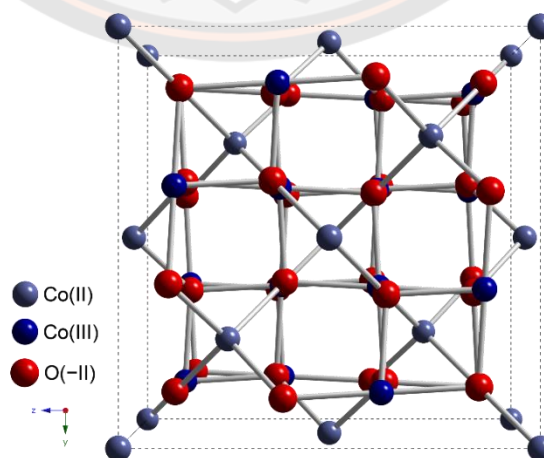


Figure 9 Cubic Co₃O₄ spinel structure (35)

Table 2 Chemical, physical, and optical properties of Co₃O₄

Chemical formula	Co ₃ O ₄
Molar mass	240.80 g/mol
Appearance	Fine dark grey to black solid
Density	6.07 g/cm ³
Melting point	895°C
Boiling point	900°C
Solubility	-Insoluble in water -Soluble (with degradation) in acids and alkalis
Crystal structure	Cubic Co ₃ O ₄ spinel structure
Band gap	1.5-2.2 eV

Cobalt oxide with spinel structure has a common structural arrangement shared by many oxides of the transition metals. Co₃O₄ is a p-type semiconductor material. It has an energy gap between 1.5-2.2 eV, which response in the visible region. This material can be applied for an important in practical visible light-induced applications such as optical catalysts, electrode anode in lithium battery, gas sensor, and photoelectric electrochemical separation. (33) Co₃O₄ with spinel structure have been used for the photocatalytic degradation of organic pollutants under visible light irradiation. (34) As shown in **Figure 9**, Co₃O₄ is a typical spinel structure with a 2:1 ratio of octahedral coordinated Co³⁺ and tetrahedral coordinated Co²⁺. (35) In Co₃O₄, there are two types of cationic sites, each of which takes up a part of the unit cell, resulting in a 56-atom unit cell. With a Co³⁺-O bond length of 1.89 and a Co²⁺-O bond length of 1.99, The electrical structure of Co₃O₄ is predicted to demonstrate a change in bonding nature (covalent or ionic nature) because of distinct Co-O bond lengths and oxidation states, and chemical shift leads to varied satellite properties and functions valence band structure. The oxidation states of cobalt (Co) in cobalt oxide form (CoO and Co₃O₄) are very sensitive to the nature of the reaction medium, temperature, and pressure. Due to its chemical and physical properties in **Table 2**, the electronic structure

and reducibility/oxidizability of these oxides form are the critical factors in determining the physical and chemical properties, such as magnetism, sensors, and catalysis.

2.7 Copper bismuth oxide (CuBi₂O₄)

CuBi₂O₄ is a tetragonal copper bismuth oxide with a three-dimensional array of [CuO₄]⁻⁶ square-planar units staggered along the c-axis and separated by Bi³⁺ ions, as seen in the **Figure 10**. The hybridizations of Bi 6s states and Cu 3d states with O 2p inside the valence and conduction bands in the ternary oxide CuBi₂O₄ are crucial variables that induce desired material features including visible-light absorption and p-type conductivity and its narrow band gap energy of 1.5-1.8 eV. CuBi₂O₄ has been found to offer potential as a material for converting solar energy into chemical fuels via photoelectrochemical (PEC) conversion. (36,37)

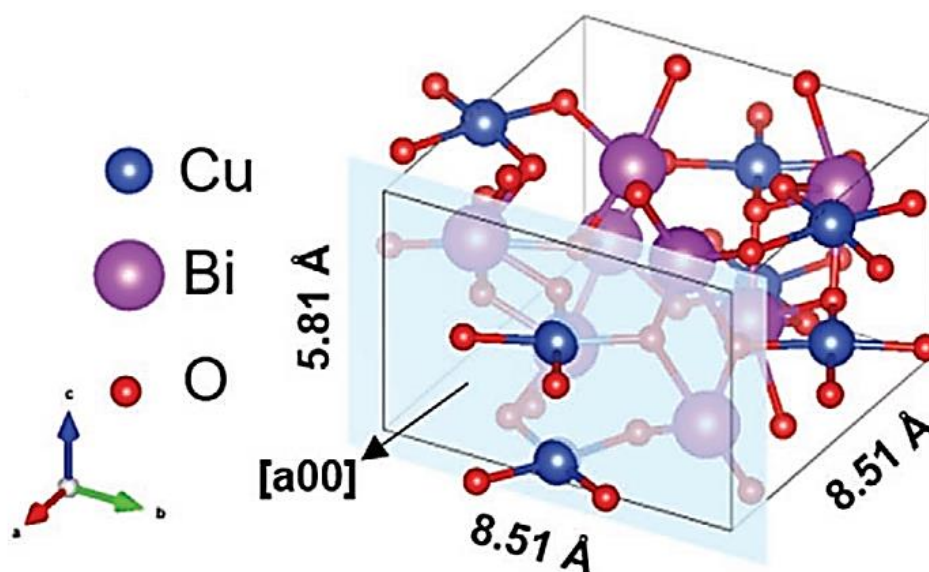


Figure 10 Tetragonal structure of CuBi₂O₄ (36,37)

Table 3 Chemical, physical, and optical properties of CuBi₂O₄

Chemical formula	CuBi ₂ O ₄ (Bi ₂ O ₃ and CuO)
Molar mass	545.50 g/mol
Appearance	Black solid
Density	7.15 g/cm ³
Melting point	N/A
Boiling point	N/A
Solubility	Insoluble in water
Crystal structure	Tetragonal
Band gap	1.5-1.8 eV

2.8 Literature Review and articles research

2.8.1 Literature Review and Articles research of Co₃O₄

In 2020, F. Khan., et al. (38) synthesized Co₃O₄ nanoparticles using a liquid-based chemical process. In this research, chemical adsorption and photocatalytic tests were performed on the NPs over safranin dye degradation. It was observed that the photocatalytic effectiveness of nanomaterials (81.40%) was highly effective for the breakdown of safranin dye after 80 minutes under UV stimulation, as shown in Figure 11. Additionally, The Co₃O₄ nanoparticles showed good stability and could be reused up to four times.

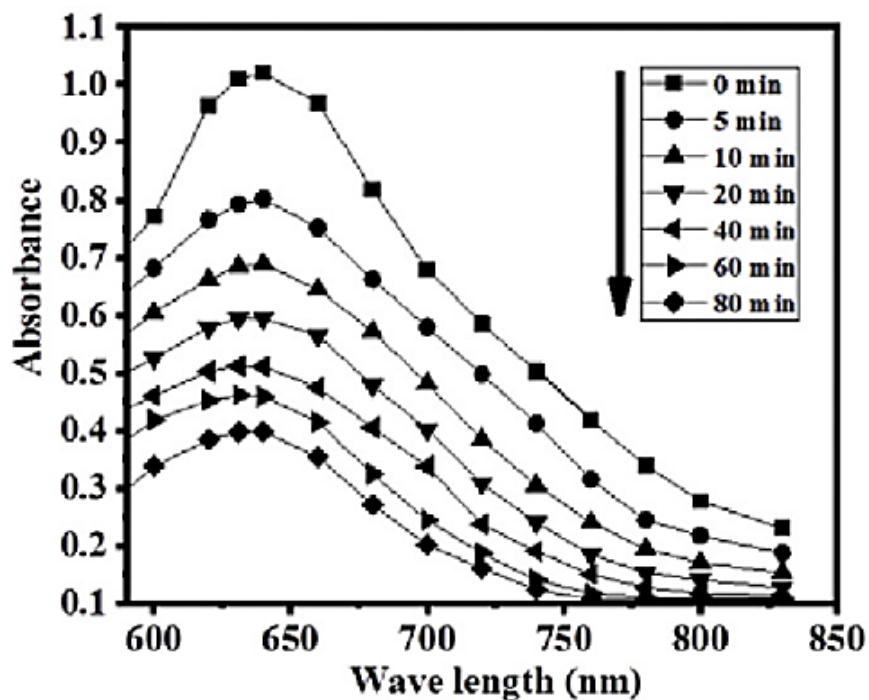


Figure 11 Absorption spectral changes with photocatalytic degradation time of SA dye (38)

In 2019, R. Ranjith et al. (39) reported the modification via green synthesis of Co_3O_4 by making as nanocomposite with reduced graphene oxide (rGO) supported $\text{TiO}_2/\text{Co}_3\text{O}_4$ for photocatalytic degradation of methylene blue and crystal violet under visible light. It was found that $\text{rGO}/\text{TiO}_2/\text{Co}_3\text{O}_4$ possessed higher photocatalytic degradation than that of pure Co_3O_4 , pure TiO_2 , and $\text{TiO}_2/\text{Co}_3\text{O}_4$ composite. A higher photocatalytic activity for dye degradation was found for the composites containing rGO. This is because rGO not only help trap electron via through π - π stacking, but also had high surface area which supported the performance of photocatalytic dyes degradation, **Figure 12**.

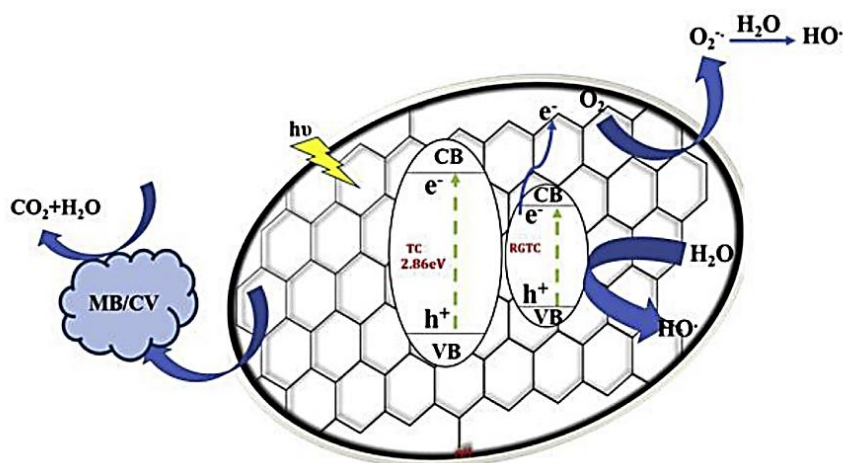


Figure 12 Degradation mechanism MB and CV by rGO-TiO₂/Co₃O₄ nanocomposite (39)

In 2021, S.P. Keerthana et al. (40) reported the influence of 1, 2 % Sn doped Co₃O₄ on Co₃O₄ photocatalyst for dye degradation. In this research, they explained that Co₃O₄ provided two different oxidation states of cobalt: Co²⁺ and Co³⁺ in which the electrons can be easily trapped by these two ions, and subsequently produced generated super oxides (⁻O₂[•]) and hydroxyl radicals (OH[•]). After doping Co₃O₄ with Sn ions, the photocatalytic activity for MB degradation of Sn-doped Co₃O₄ was found to be higher than that of the pure one. The new energy levels created by Sn metal ions within a band gap of the Co₃O₄ act as an electron trap, and the recombination step should be retarded. As shown in **Figure 13**, 2% Sn-doped Co₃O₄ is the optimum level of doping with the best performance towards degrading methylene blue dye. Therefore, 2% Sn-doped Co₃O₄ might be suitable candidate for removing organic pollutants in waste water and helpful in water treatment process as this material is less toxic in nature and more efficient.

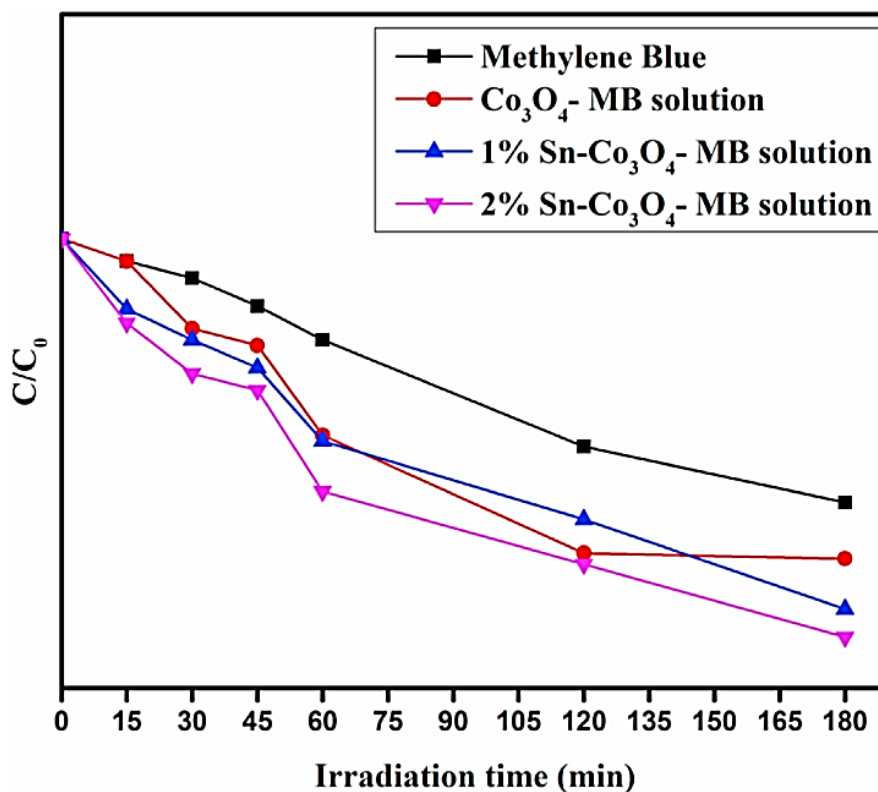


Figure 13 Graph plot of C/C_0 Vs time of photocatalyst in MB solution (40)

In 2021, C. Arunachalam et al. (41) reported the preparation of the binary heterojunction $MnFe_2O_4-Co_3O_4$ nano-photocatalyst (NCs) by sonochemical method. UV-vis DRS revealed a shift in the bandgap of $MnFe_2O_4$ (1.8 eV) and Co_3O_4 (2.86 eV) for $MnFe_2O_4-Co_3O_4$ from 2.86 eV to 2.47 eV, allowing for improved visible light harvesting. The efficiency of MB dye degradation reveals that $MnFe_2O_4-Co_3O_4$ has high recycling and photo-corrosion resistance, and photocatalytic performance, as shown in **Figure 14**. The percentage of dye degradation in presence of 3 mg of $MnFe_2O_4-Co_3O_4$ NCs at 200 min was 80% compared to $MnFe_2O_4$ (31%) and Co_3O_4 (26%). They found that the OH^- and h^+ ions were important in the breakdown of the MB dye in this study. $MnFe_2O_4-Co_3O_4$ photocatalyst not only provided photocatalytic activity, but it also applied as application of antimicrobial agents against *Escherichia coli* and *Bacillus subtilis*. The modification of Co_3O_4 by adding $MnFe_2O_4$ could be a

promising photocatalytic option for applications such as pollution degradation and antibacterial applications.

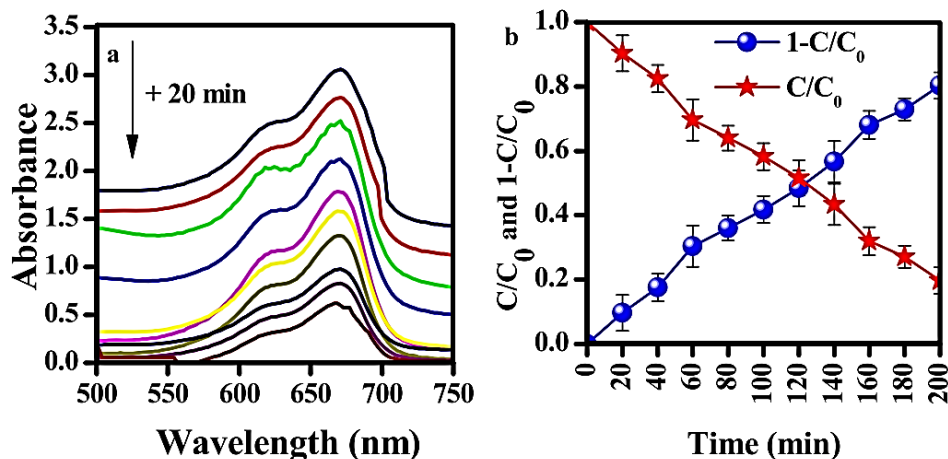


Figure 14 (a) UV-vis spectral change of MB dye after addition of $\text{MnFe}_2\text{O}_4\text{-Co}_3\text{O}_4$ (b) The plot of C/C_0 and $1-(C/C_0)$ versus time after addition of $\text{MnFe}_2\text{O}_4\text{-Co}_3\text{O}_4$ (41)

2.8.2 Literature review and articles research of CuBi_2O_4

In 2013, Y. Xie et al. (42) reported the preparation of leaf-like CuBi_2O_4 with various novel morphologies via a hydrothermal process. It was found that the concentration of $\text{Cu}(\text{NO}_3)_2$ -to- NaOH molar ratio and the Cu^{2+} affected the variation of morphologies of CuBi_2O_4 . The different morphologies of CuBi_2O_4 with various parameters such as pH, hydrothermal temperature and reaction time were also presented in **Figure 15**. Based on the results, leaf-like CuBi_2O_4 nanosheets with a uniform spinel phase demonstrated enhanced photocatalytic degradation of MB under visible light irradiation over the presence of H_2O_2 .

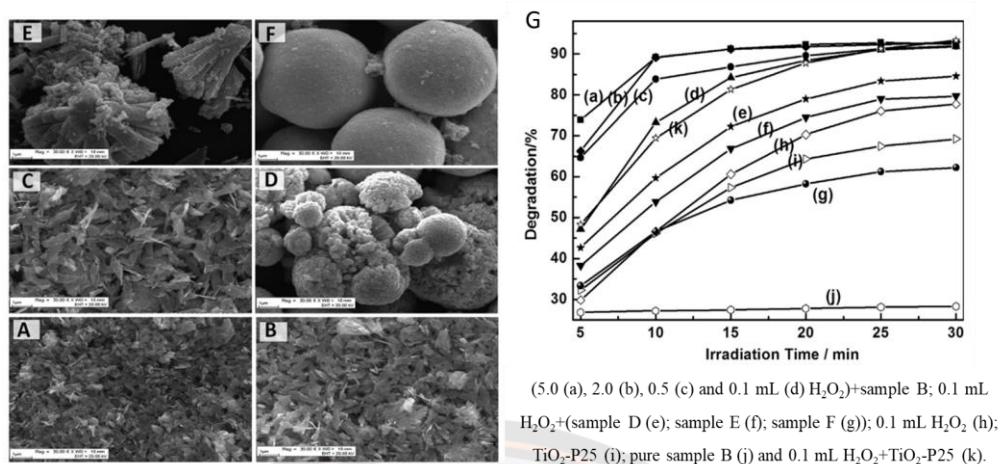


Figure 15 SEM images of the samples prepared at 120 °C for 6 h (A), 12 h (B, D, E, F) and (G) Effects of CuBi₂O₄ on the photocatalytic oxidation of MB under 500-W xenon lamp irradiation

In 2015, A. Elaziouti et al. (43) reported the preparation and characterization of novel CuBi₂O₄/SnO₂ p–n heterojunction with enhanced photocatalytic performance of congo red (CR) degradation under UVA light irradiation. They found that 5 wt% CuBi₂O₄/SnO₂ photocatalyst exhibited higher photocatalytic efficiency, as compared to the single phases CuBi₂O₄ and SnO₂ after 100 min irradiation. According to the band edge position, the electronic potential of the conduction band of n-SnO₂ is slightly more anodic than that of p-CuBi₂O₄, whereas, the hole potential of the valence band top of n-SnO₂, is more positive than that of p-CuBi₂O₄. Therefore, the probabilities of electron–hole recombination would be decreased. The increase in photocatalytic activity of CuBi₂O₄/SnO₂ would be efficient to the suppression of electron–hole recombination by the effective electron separation, as shown in **Figure 16**.

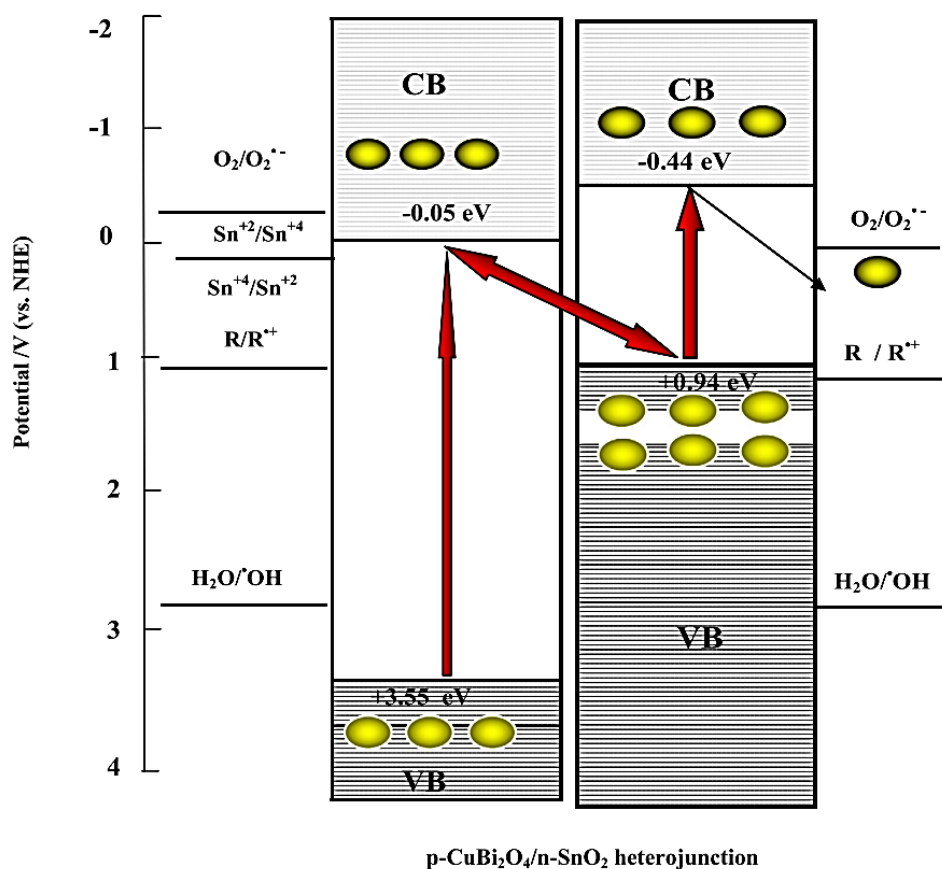


Figure 16 Proposed photocatalytic degradation mechanism and the energy level alignment (43)

In 2020, H. Ramezanalizaadeh et al. (44) modified CuBi₂O₄ by the fabrication of CoTiO₃/CuBi₂O₄ heterojunction for degradation of DR16 dye. As shown in **Figure 17**, as-synthesized CoTiO₃/CuBi₂O₄ heterojunction shows the highest percentage of degradation under visible light due to the suitable heterojunction formation and synergistic effect between separate CoTiO₃ and CuBi₂O₄ nanostructure.

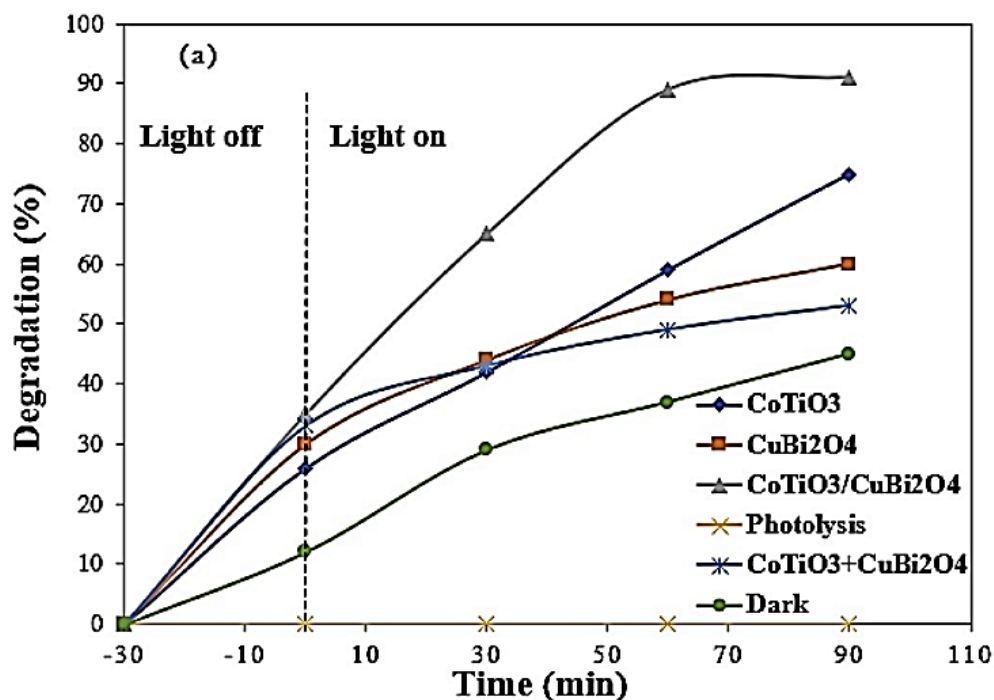


Figure 17 Photocatalytic degradation of DR16 over different photocatalysts (44)

In 2020, M. Sabri. et al. (45) prepared and modified CuBi_2O_4 by making heterostructures with ZnO ($\text{ZnO}/\text{CuBi}_2\text{O}_4$) for photocatalytic degradation of dye contaminants under visible light. According to, the outcomes indicated that with increasing weight percentage of CuBi_2O_4 up to 5.0 %, photodegradation of rhodamine B (RhB) showed highly efficiency within 210 min. After 1.48 mM of potassium persulfate was added, the rate of RhB showed effectively degraded after 210 min under visible light. The improved in photocatalytic reaction over the $\text{ZnO}/\text{CuBi}_2\text{O}_4$ composites attributed to the charge transfer between the ZnO and CuBi_2O_4 . The electrons on CB of CuBi_2O_4 would migrate to CB of ZnO , while holes in VB of ZnO transferred the VB of CuBi_2O_4 . As a result, the separation of charge carriers is impressively increased. After add persulfate in the system, persulfate can decompose to produce some sulfate anions radical ($\cdot\text{SO}_4^-$), but also can react with Cu^{2+} to produce Cu^{3+} and sulfate anions radical ($\cdot\text{SO}_4^-$) and sulfate anions radical ($\cdot\text{SO}_4^-$) can react with water to generate hydroxyl radical ($\text{OH}\cdot$), as show in **Figure 18**. Therefore, the synergistic effect of persulfate and the heterojunction formation in the $\text{ZnO}/\text{CuBi}_2\text{O}_4$

nanocomposite have a significant influence on the separation of the charges and also a considerable role in the enhancement of the photocatalytic performance of the ZnO/CuBi₂O₄ heterojunction photocatalyst. Based on the reported literature, it can be concluded that the photocatalytic efficiency of various pollutants by different CuBi₂O₄ and Co₃O₄-based photocatalysts were higher than that of the single photocatalyst.

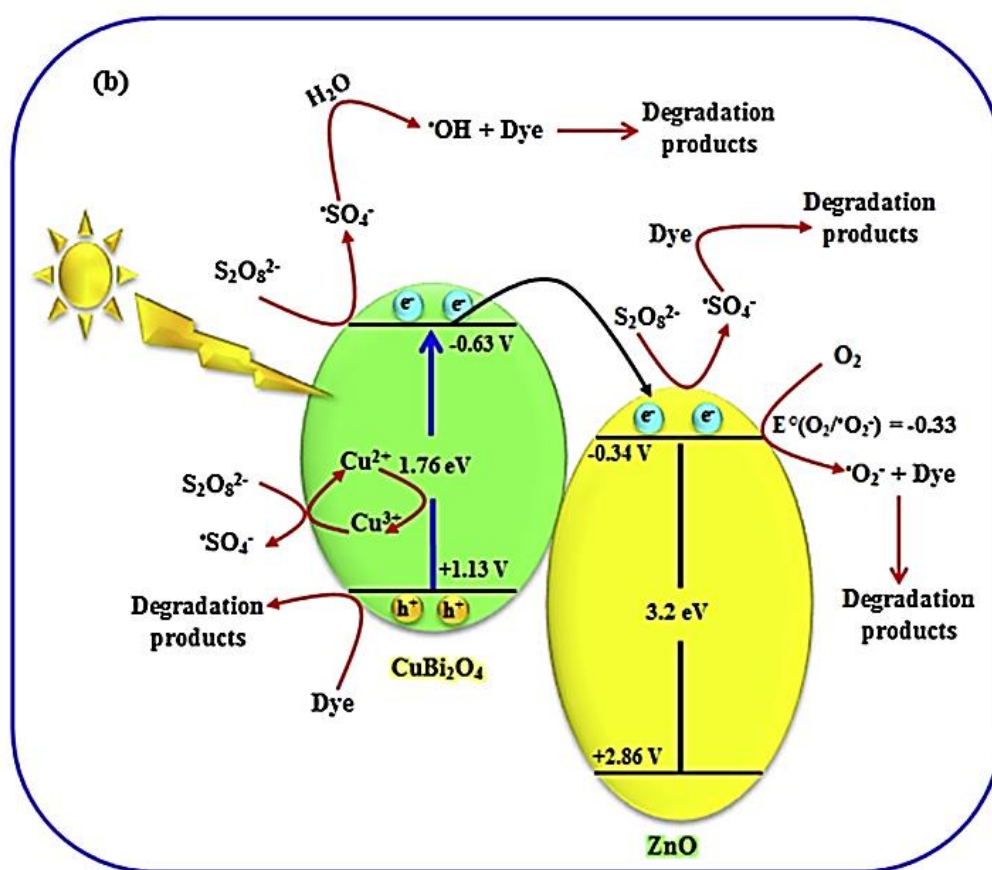


Figure 18 Schematic of photocatalytic reaction over the ZnO/CuBi₂O₄/PS system (45)

As with the reports reviewed above, it could be observed that CuBi₂O₄ and Co₃O₄-based composites are more active than its individual photocatalysts. Therefore, the development of photocatalysts in this work is required to develop high-performance CuBi₂O₄/Co₃O₄ composites. In this project, a facile and straightforward strategy is designed to prepare Co₃O₄ composite with CuBi₂O₄ and compare with that of pure photocatalyst for the photocatalytic degradation of contaminants (MB dyes) under

visible light irradiation. The results expected for the synthesis of composites is to promote the separation of charge carriers, the increase the photocatalytic efficiency. However, the significantly enhanced photocatalytic performance of composites is dependent on the amount of Co_3O_4 adding in the coupling between CuBi_2O_4 and Co_3O_4 .



CHAPTER III

RESEARCH METHODOLOGY

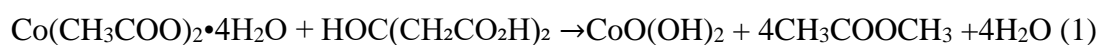
3.1 Chemicals and reagents

All the chemicals have an analytical purity and were used as received, without further purification. Herein, cobalt (II) acetate tetrahydrate, citric acid, copper (II) nitrate trihydrate, bismuth (III) nitrate pentahydrate, ethylene glycol (EG), iso-propanol, sodium hydroxide, and distilled water were used for the preparation of the photocatalysts.

3.2 Synthesis of photocatalyst

3.2.1 Preparation of cobalt (II) oxide (Co₃O₄)

Co₃O₄ was prepared by co-precipitation method. In a typical, cobalt (II) acetate tetrahydrate (0.05 M) was dissolved in 60 ml ethylene glycol under vigorous magnetic stirring. Citric acid was dissolved in iso-propanol 60 ml under vigorous magnetic stirring. Then the citric acid solution was slowly dropped wise to cobalt (II) acetate solution continuous stirring for 30 min to form a homogeneous solution. Then, the precipitating agent 0.1 M NaOH (100 ml) was added dropwise into the mixture under continuous stirring for 6 h at 60°C. The precipitate was filtered using centrifugation machine (5000 rpm, 5 min), washed with DI water for several time, and dried at 100°C for 12 h in a hot air oven. After that, the black powder of Co₃O₄ was obtained after calcination at 600°C for 2 h. A summary of preparation of Co₃O₄ via co-precipitation method is shown in **Figure 19**.



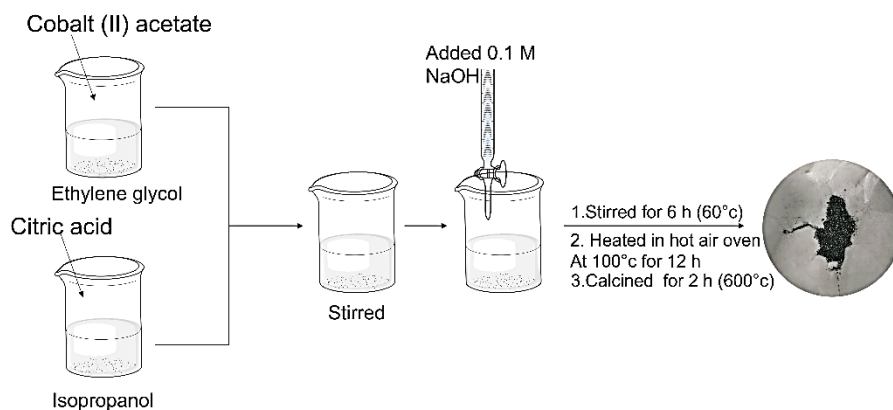


Figure 19 Preparation of Co_3O_4 via co-precipitation method

3.2.2 Preparation of copper bismuth oxide (CuBi_2O_4)

Steps of preparation of CuBi_2O_4 by co-precipitation method are shown in **Figure 20**. In a typical, copper (II) nitrate trihydrate (0.05 M) and bismuth (III) nitrate pentahydrate (0.05 M) was dissolved separately in 25 ml DI water with continuous stirring for 30 min. All mixed solutions were adjusted to a constant pH value of 14 by 2 M NaOH and continuously stirred for 10 h. The filtered powders were washed and dried at 100°C for 2 h. The obtained CuBi_2O_4 powders were then calcined at 600°C for 3 h.



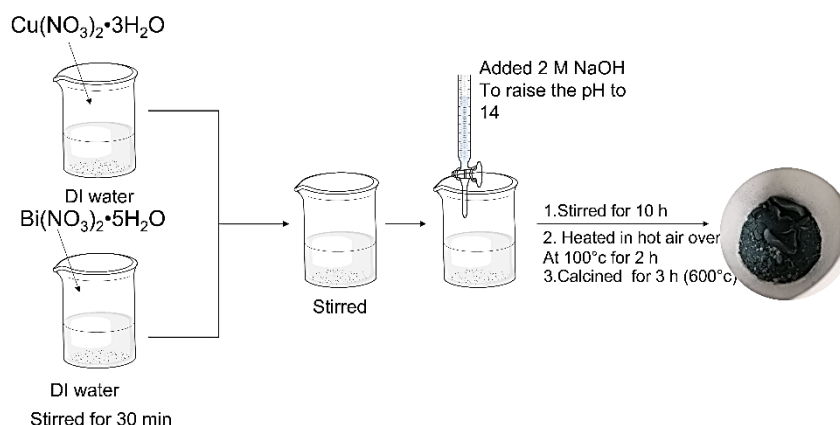


Figure 20 Preparation of CuBi_2O_4 via co-precipitation method

3.2.3 Preparation of $\text{Co}_3\text{O}_4/\text{CuBi}_2\text{O}_4$ composites

$\text{Co}_3\text{O}_4/\text{CuBi}_2\text{O}_4$ composites with different amounts of Co_3O_4 (20% wt, 50% wt, and 80% wt.) were prepared according to the same procedure with preparation of CuBi_2O_4 , as shown in **Figure 21**. Before adjusting the pH value of the mixture to 14, different amounts of Co_3O_4 powders were added to the above solution. The calculated values of Co_3O_4 powder are shown in **Table 4**. The Co_3O_4 particles were kept dispersed in the mixed suspensions and stirred for 10 h at room temperature. After stirring, the $\text{Co}_3\text{O}_4/\text{CuBi}_2\text{O}_4$ composites were collected, washed and then dried at 100 °C for 2 h. Then the produced $\text{Co}_3\text{O}_4/\text{CuBi}_2\text{O}_4$ composites were again calcined at 600°C for 3 h.

Table 4 Preparation of $\text{Co}_3\text{O}_4/ \text{CuBi}_2\text{O}_4$ composite weight percent of CuBi_2O_4

Photocatalyst	Amount of CuBi_2O_4 (g)	Amount of Co_3O_4 (g)
20 wt% $\text{Co}_3\text{O}_4/\text{CuBi}_2\text{O}_4$		0.04
50 wt% $\text{Co}_3\text{O}_4/\text{CuBi}_2\text{O}_4$	0.20	0.10
80 wt% $\text{Co}_3\text{O}_4/\text{CuBi}_2\text{O}_4$		0.16

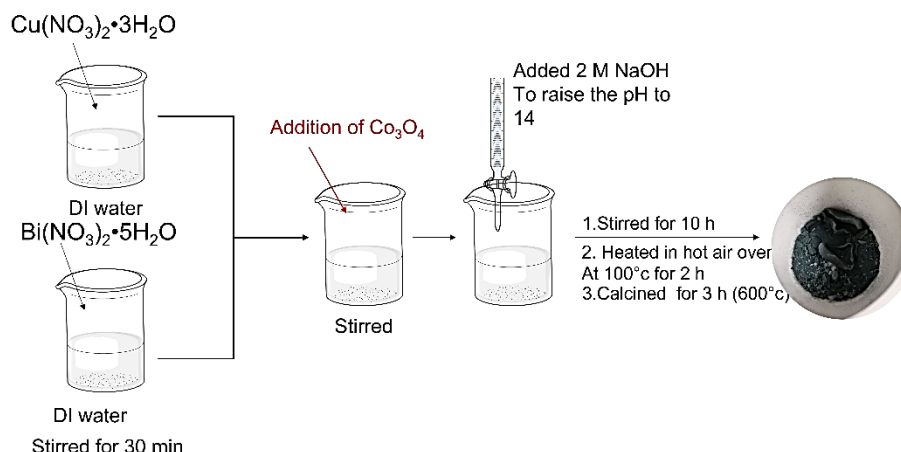


Figure 21 Preparation of $\text{Co}_3\text{O}_4/\text{CuBi}_2\text{O}_4$ composites

3.3 Material characterizations

- Crystallographic structures and phase composition were detected by an X-ray diffraction instrument (XRD, Philips X'PertMPD).

- The morphologies were studied using a scanning electron microscope (SEM, JSM-6335F, JEOL) equipped with energy dispersive X-ray spectrometer (EDS) for elemental analysis.

- Transmission electron microscope (TEM, JSM-2010, JEOL) was used to examine the morphologies and the particle size with two-dimensional images.

- The specific surface area was determined from N_2 adsorption/desorption isotherms based on the Brunauer–Emmett–Teller (BET) theory (Micromeritics TriStar II 3020).

- The photoluminescence (PL) spectrophotometer excited with a 350 nm light source was used for analyzing the emission wavelength (Fluoromax-4 Horiba JobinYvon) at room temperature.

- Optical studies for reflectance, absorbance and band gap analysis were analyzed using diffuse reflectance spectra (DRS) on a UV–vis spectrophotometer (Shimadzu, UV-3101PC).

3.4 Photocatalytic degradation

The photocatalytic activities were conducted by adding 0.05 g of the prepared photocatalysts into 50 ml of 3 ppm (C_0) methylene blue (MB) solution. Before the light irradiation the solution was stirred for 30 min in the dark. Under visible light irradiation, the photocatalytic degradation of MB was studied in home-made photoreactor combined with 18 W halogen lamp (visible light). Under light irradiation is attributed, the 3 ppm of MB solution was collected every at 30 minutes time interval (0, 30, 60, 90, and 120 min). The remaining concentration of MB dye in solution (C_t) at the wavelength of 664 nm was evaluated using a double beam UV-visible spectrophotometer (Shanghai Mapada Instruments Co., Ltd.). Summary of some photocatalysts tested in this study is shown in **Figure 22**.

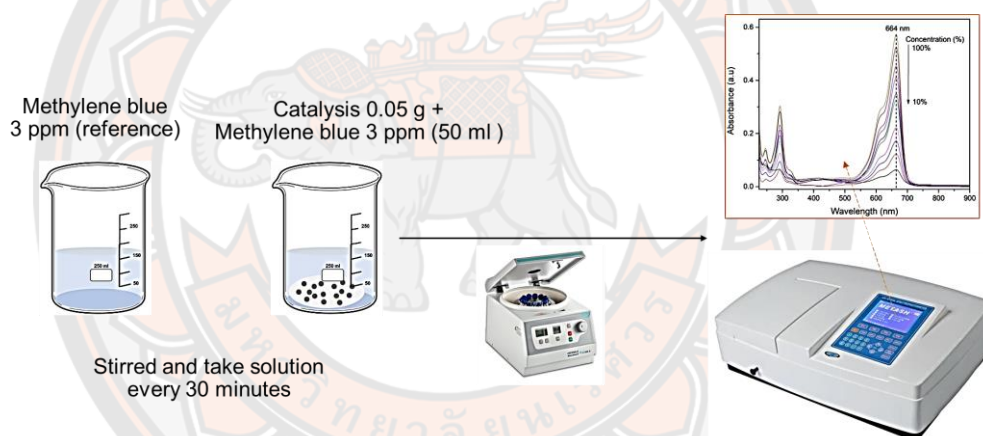


Figure 22 Photocatalytic degradation of $\text{Co}_3\text{O}_4/\text{CuBi}_2\text{O}_4$ composites.

The absorbance (A) of the MB solution is then converted to calculate the remaining concentration (C_t) using the equation for the standard curve (Beer Lambert Law). A linear calibration curve was (in **Figure 23**.) conducted by preparing a series of known MB concentrations (0, 1, 2, 3, 4, and 5 ppm).

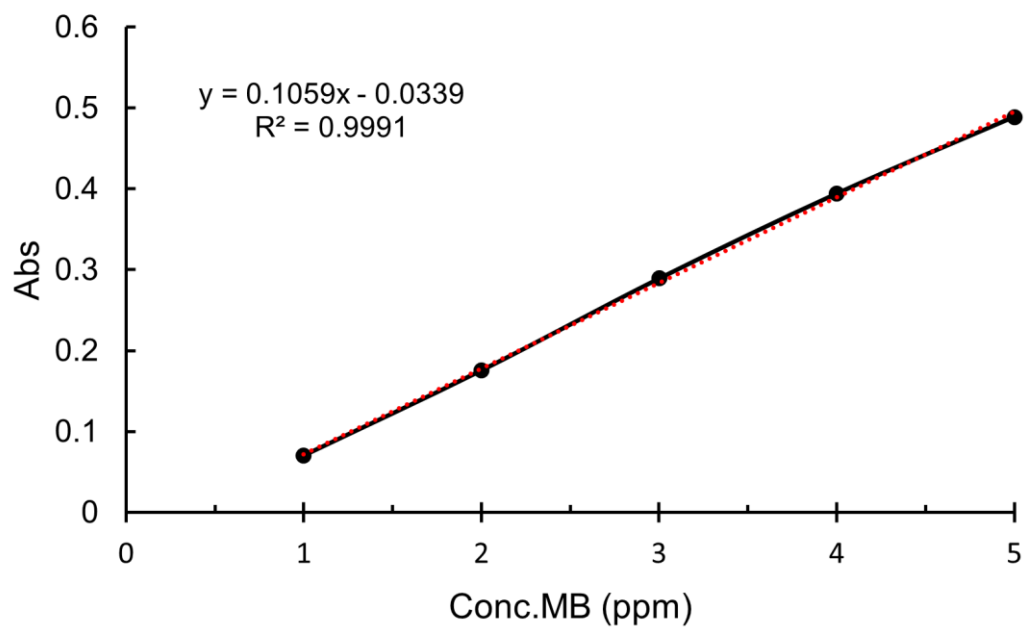
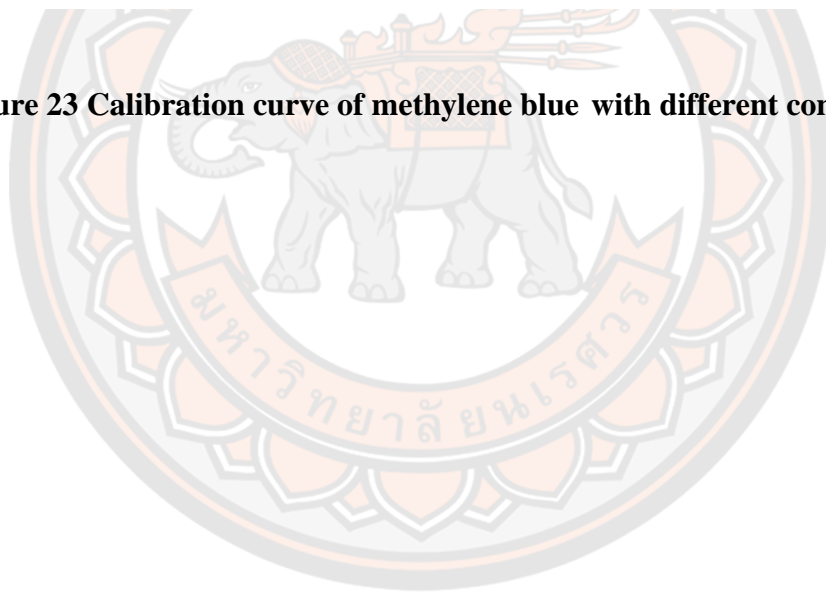


Figure 23 Calibration curve of methylene blue with different concentrations



CHAPTER IV

RESULTS AND DISCUSSION

4.1 X-ray diffraction technique (XRD)

4.1.1 X-ray diffraction of Co_3O_4

Pure Co_3O_4 powders for XRD analysis were synthesized by co-precipitation and calcining at 600°C for 2 hours. **Figure 24** shows the XRD pattern of Co_3O_4 XRD patterns around 2θ at 19.0° , 31.3° , 36.8° , 38.5° , 44.8° , 55.6° , 59.3° , and 65.2° . All eight diffraction main peaks can be assigned to the (111) (220) (311) (222) (400) (422) (511) and (440) planes respectively, which are in good agreement with the cubic Co_3O_4 spinel structure (JCPDS no.01-073-1701) with the lattice constant ($a=8.08350 \text{ \AA}$) (46).

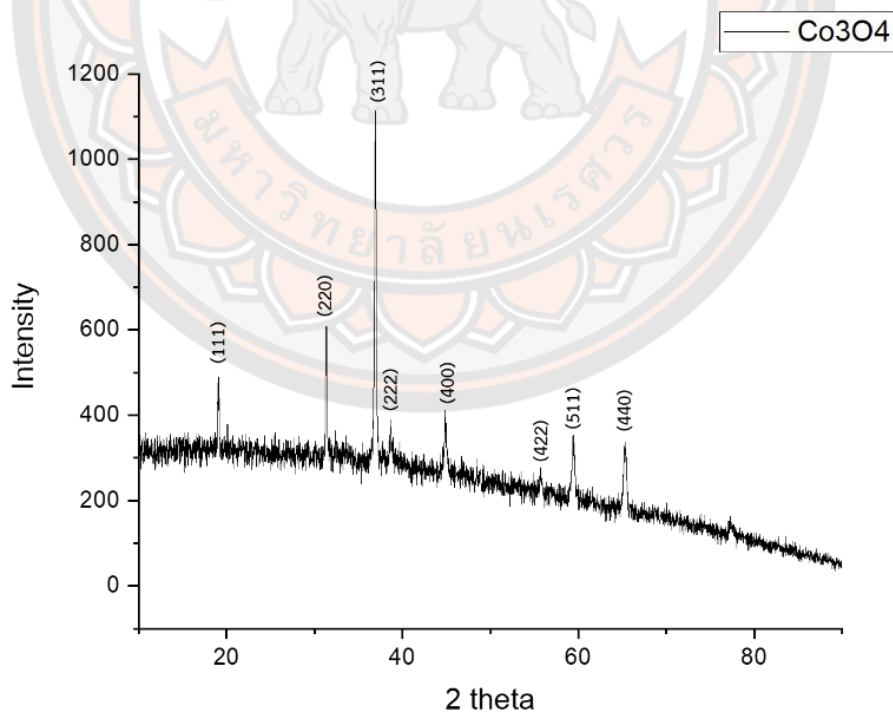


Figure 24 XRD pattern of Co_3O_4

4.1.2 X-ray diffraction of CuBi_2O_4 .

In this part, pure CuBi_2O_4 powders was prepared by co-precipitation and then calcined at 600°C for 3 hours before XRD analysis. In **Figure 25**, the 2θ peaks at 20.88° , 28.01° , 29.72° , 30.72° , 32.51° , 33.13° , 34.21° , 37.44° , 45.22° , 45.94° , 46.72° , 47.82° , 53.34° , 55.66° , 61.68° , 63.80° , 66.11° , 73.05° , 74.41° , and 77.79° corresponding to the hkl plane (200), (211), (220), (002), (102), (310), (112), (202), (330), (312), (411), (420), (402), (332), (402), (332), (440), (530), (413), (541), (602), and (523), respectively. This is consistent with the value given in the standard JCPDS file no.00-42-0334 with the lattice constants of $a=b=8.4996\text{ \AA}$ and $c=5.8172\text{ \AA}$ (47).

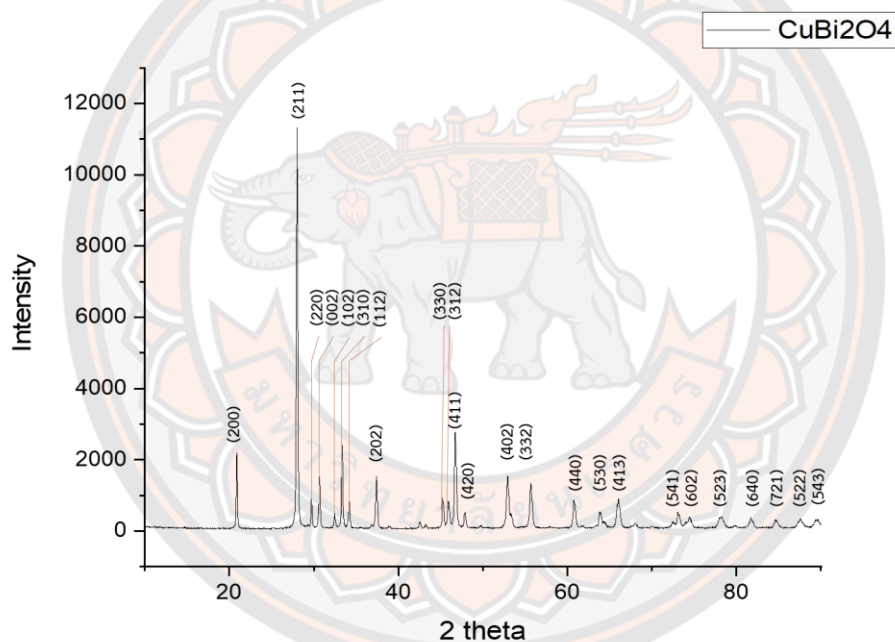


Figure 25 XRD pattern of tetragonal structure CuBi_2O_4

4.1.3 X-ray diffraction of $\text{Co}_3\text{O}_4/\text{CuBi}_2\text{O}_4$ composites

X-ray diffraction technique of $\text{Co}_3\text{O}_4/\text{CuBi}_2\text{O}_4$ composite after calcining at 600°C for 3 hours is presented in **Figure 26**. The obtained all diffraction peaks of $\text{Co}_3\text{O}_4/\text{CuBi}_2\text{O}_4$ composites showed the existence of mixed phases of cubic Co_3O_4 and tetragonal CuBi_2O_4 in all the tested, while the CuBi_2O_4 diffraction peaks were noticeably more intense.

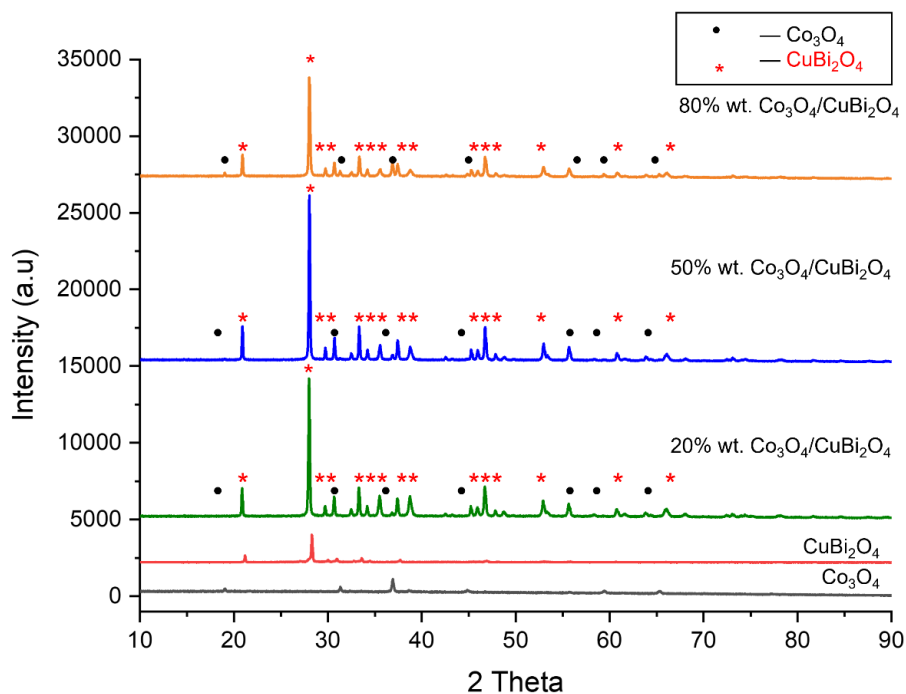


Figure 26 The XRD patten of $\text{Co}_3\text{O}_4/\text{CuBi}_2\text{O}_4$ composites

4.2 The Brunauer–Emmett–Teller, BET

The surface properties including specific surface area, pore volume, and average pore size diameter of the prepared photocatalyst are listed in **Table 5**. It was found that the specific surface area of Co_3O_4 was $4.5418 \text{ m}^2/\text{g}$, while CuBi_2O_4 was $4.4346 \text{ m}^2/\text{g}$. After coupling Co_3O_4 with CuBi_2O_4 , the specific BET specific surface area and pore volume of composites were increased following the order $20\% > 50\% > 80\%$ wt $\text{Co}_3\text{O}_4/\text{CuBi}_2\text{O}_4$. An increase in the units of area per sample mass (m^2/g) of the obtained composite due to the addition of Co_3O_4 or CuBi_2O_4 to the composites could suppress the grain growth of crystal leading the *small size*, which was approved with SEM images. As a result, when the particle size of photocatalyst decreases the specific surface area increases, leading to a larger number of surface-active sites that facilitates

the interaction and adsorption rate of pollutant molecules such as MB on suspended photocatalyst particles.

In **Figure 27.**, the adsorption-desorption isotherms of the pure photocatalysts and composite samples exhibited type IV isotherm with a hysteresis loop at a relative pressure (P/P_0) in the range 0.9 – 1.0, which indicated the presence of mesopores with the size distribution in the range of 2-5 nm (48) (see **Table 5**). The capacity of pore volume (cm^3/g) related to the size of a hysteresis loop. Herein, mesoporous 80% wt. $\text{Co}_3\text{O}_4/\text{CuBi}_2\text{O}_4$ showed large hysteresis loop, indicating the high capacity of pore volume ($\sim 0.0064 \text{ cm}^3/\text{g}$).

Table 5 The analysis of specific surface area, pore volume and pore size

Sample	BET surface area (m^2/g)	Pore volume (cm^3/g)	Pore size (nm)
Co_3O_4	4.5418	0.0039	4.83
CuBi_2O_4	4.4346	0.0041	4.51
20% wt. $\text{Co}_3\text{O}_4/\text{CuBi}_2\text{O}_4$	4.8893	0.0049	4.34
50% wt. $\text{Co}_3\text{O}_4/\text{CuBi}_2\text{O}_4$	5.0066	0.0052	4.41
80% wt. $\text{Co}_3\text{O}_4/\text{CuBi}_2\text{O}_4$	6.3738	0.0064	5.15

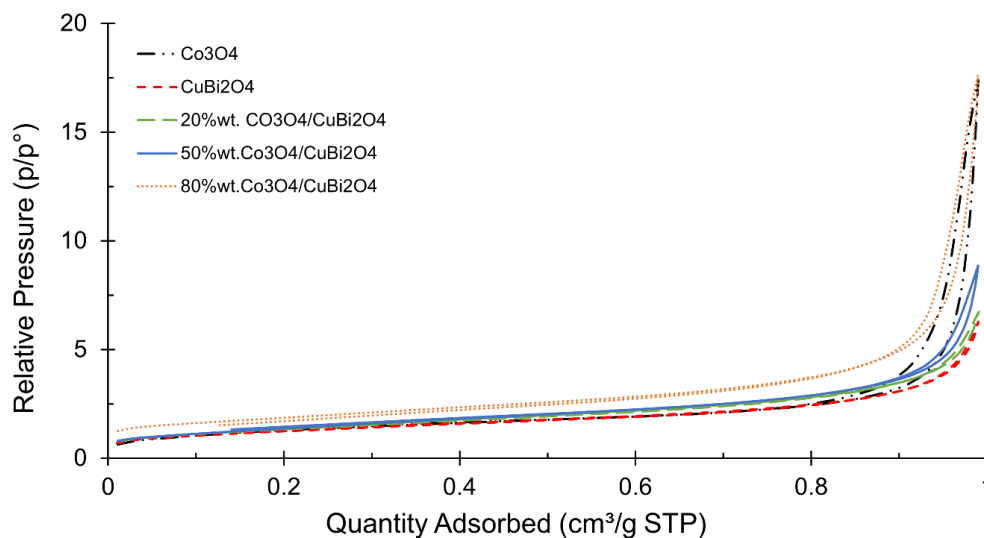


Figure 27 The nitrogen adsorption-desorption isotherm of the as-synthesized photocatalyst

4.3 Transmission electron microscope technique, TEM

TEM analysis provided a more magnified structural information with two-dimensional (2D) images of the pure sample in comparison to the composite samples. By establishing an image from a sample, the electron penetration through the sample substance was measured at a magnification of 250,000 times.

As shown in **Figure 28(a)**, TEM image showed that of the Co_3O_4 had a larger spherical particles or irregular aggregates with an average size ~ 100 nm. The appearance of CuBi_2O_4 in **Figure 28 (b)** was a sheet-like shape with a size of around 660 nm. The TEM results of the composite samples are given in **Figure 28 (c) to Figure 28 (e)**. The morphology of $\text{Co}_3\text{O}_4/\text{CuBi}_2\text{O}_4$ composites showed mixing morphology of two materials, which was attributed to the well-dispersed Co_3O_4 particles on surface of a shape sheet CuBi_2O_4 . However, when the increase amount of Co_3O_4 loading, spherical Co_3O_4 aggregates appeared as a major morphology in 80%wt. $\text{Co}_3\text{O}_4/\text{CuBi}_2\text{O}_4$ composite.

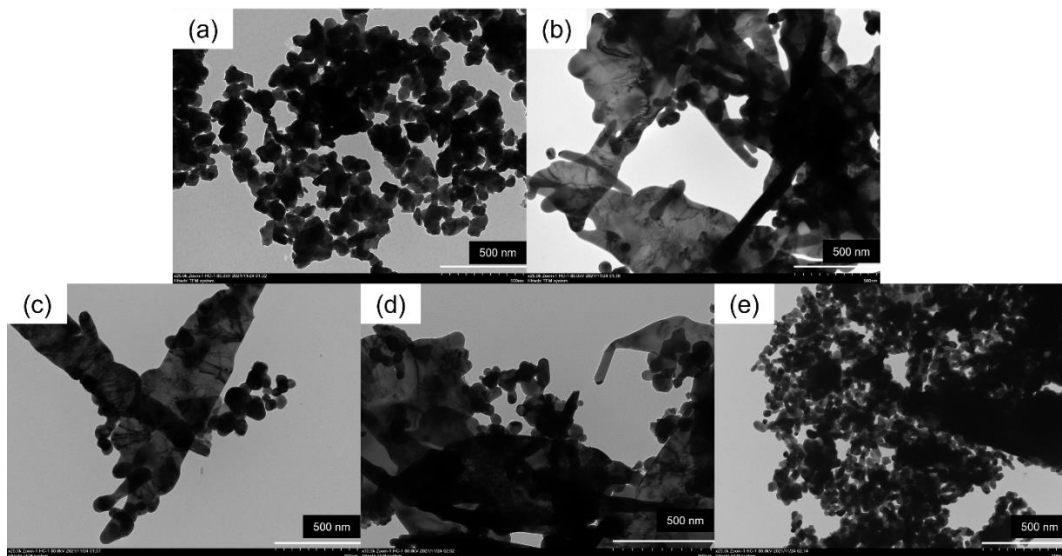


Figure 28 TEM images of (a) Co_3O_4 , (b) CuBi_2O_4 , (c) 20%, (d) 50%, and (e) 80%wt. $\text{Co}_3\text{O}_4/\text{CuBi}_2\text{O}_4$

4.4 Scanning electron microscope technique, SEM

SEM analysis provided more information about surface morphology of the pure samples compared to other composites magnifying up to 500,000 times. As shown in **Figure 29 (a)**, these aggregates Co_3O_4 had spherical morphology with the aggregation of spherical particles with size parameters around $0.15 \mu\text{m}$, while the appearance of CuBi_2O_4 had a sheet-like shape with a length of around $0.76 \mu\text{m}$ (see **Figure 29.9 (b)**). The SEM results of composites are given in **Figure 29 (c) to Figure 29 (e)**. The results exhibited mixture of Co_3O_4 and CuBi_2O_4 phases by the dispersion of Co_3O_4 particles supported on the surface of CuBi_2O_4 sheets.

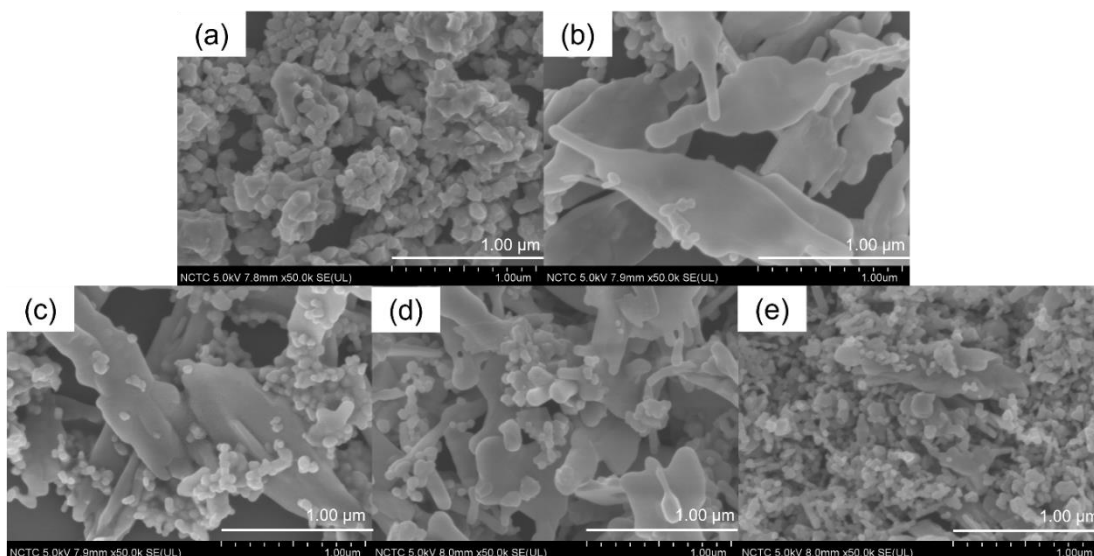


Figure 29 SEM images of (a) Co_3O_4 , (b) CuBi_2O_4 , (c) 20%, (d) 50% and (e) 80%wt. $\text{Co}_3\text{O}_4/\text{CuBi}_2\text{O}_4$

4.5 Photoluminescence spectroscopy (PL)

Photoluminescence is employed to investigate the efficiency of photoexcited charge transfer, immigration, trapping and electron-hole recombination of Co_3O_4 , CuBi_2O_4 and $\text{Co}_3\text{O}_4/\text{CuBi}_2\text{O}_4$ composites. The PL spectra of Co_3O_4 , CuBi_2O_4 and $\text{Co}_3\text{O}_4/\text{CuBi}_2\text{O}_4$ composites are shown in **Figure 30A** lower intensity of the PL signal in $\text{Co}_3\text{O}_4/\text{CuBi}_2\text{O}_4$ composites compared to unmodified photocatalysts implies the less electron relaxation to ground state, which indicated the decrease in electron-hole recombination rate.

Making heterojunction between Co_3O_4 and CuBi_2O_4 may improve the charge separation through a favorable type-II heterojunction (staggered gap), and finally improve photoactivity (see **Figure 31**).

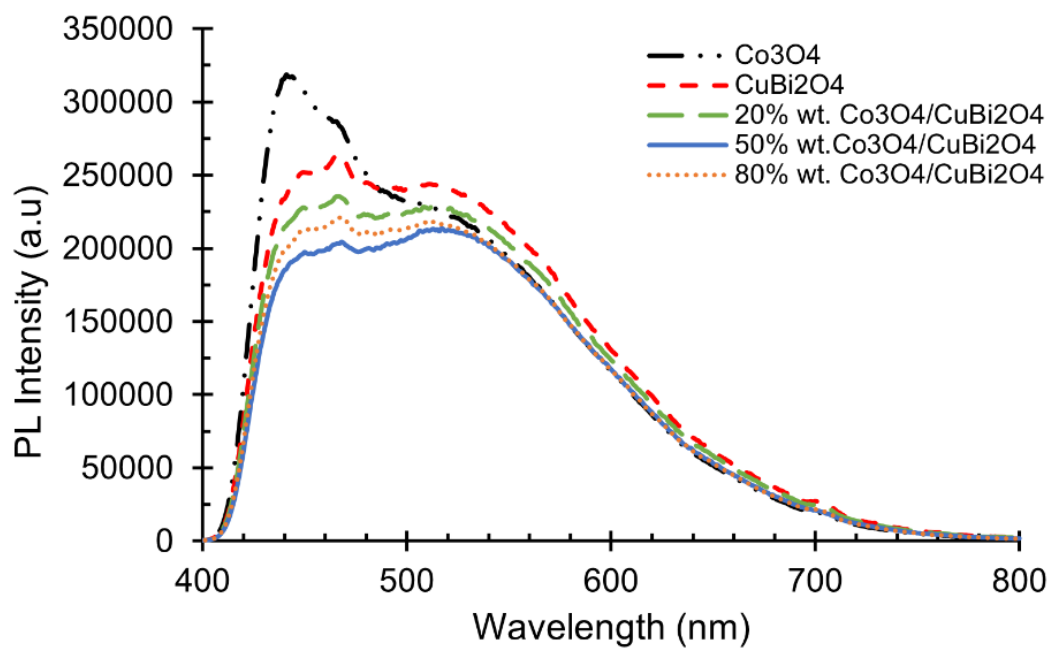


Figure 30 PL spectra of pure Co_3O_4 , pure CuBi_2O_4 and $\text{Co}_3\text{O}_4/\text{CuBi}_2\text{O}_4$ composites

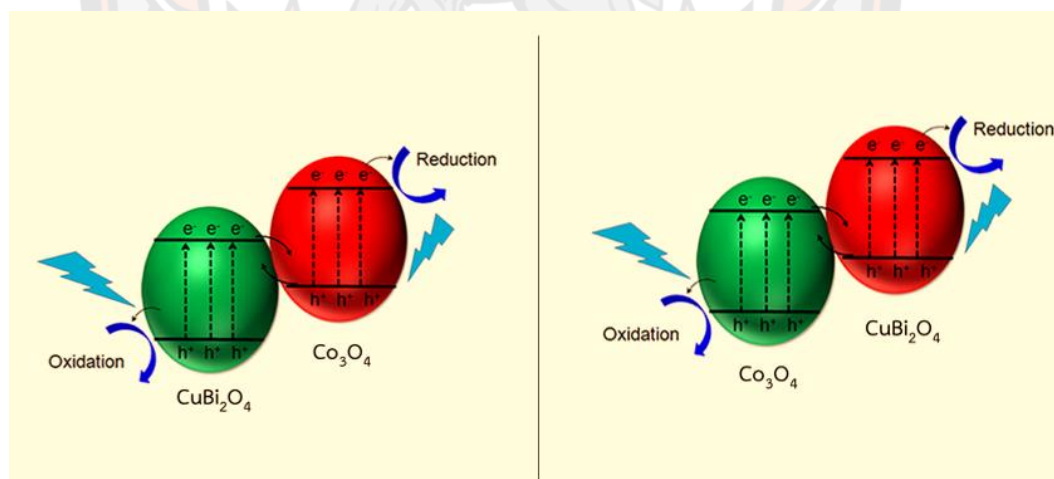


Figure 31 Charge separation through a type-II heterojunction of $\text{Co}_3\text{O}_4/\text{CuBi}_2\text{O}_4$ composites

4.6 Diffuse reflectance spectroscopy, DRS UV/Vis

Since photocatalytic processes occurring in heterogeneous systems, thus the absorption spectrum can be derived from a reflection spectrum or scattering. Diffuse

reflectance spectra of pure Co_3O_4 , CuBi_2O_4 and composites in **Figure 32. (a)** were further converted in to Kubelka-Munk absorption function (**Figure 32. (b)**). The calculations of absorption values are described using the Kubelka-Munk reflectance theory, as shown in equation (1) (49).

$$F(R) = \frac{(1-R)}{2R} \quad (1)$$

where $F(R)$ = Kubelka-Munk absorption function (adsorption values)

R = Reflectance value ($R/100$)

It was found that all synthesized photocatalysts can absorb light in the visible region (> 400 nm). The optical band gap energy in Figure 32 (c) is evaluated by extrapolating the linear part of the curve and extrapolate a straight line until it intersects the baseline in x-axis. The intersection value (photon energy in eV) is the band gap according to Tauc's model (50). As listed in Table 6, absorption edge (nm) of photocatalyst corresponds to the threshold of charge transition between CB and VB and related with the required photon energy for excitation of an electron.

Band gap energy are calculated by Tauc plot which are 2.0 eV and 2.7 eV for Co_3O_4 and CuBi_2O_4 , respectively. The bandgap of composite samples lies in the range of 2.5-2.8 eV, which was closed to the value of CuBi_2O_4 host material. In this investigation, making composites does not affect the optical properties of the pure photocatalyst. Therefore, the optical properties that is measured in all samples could be neglected.

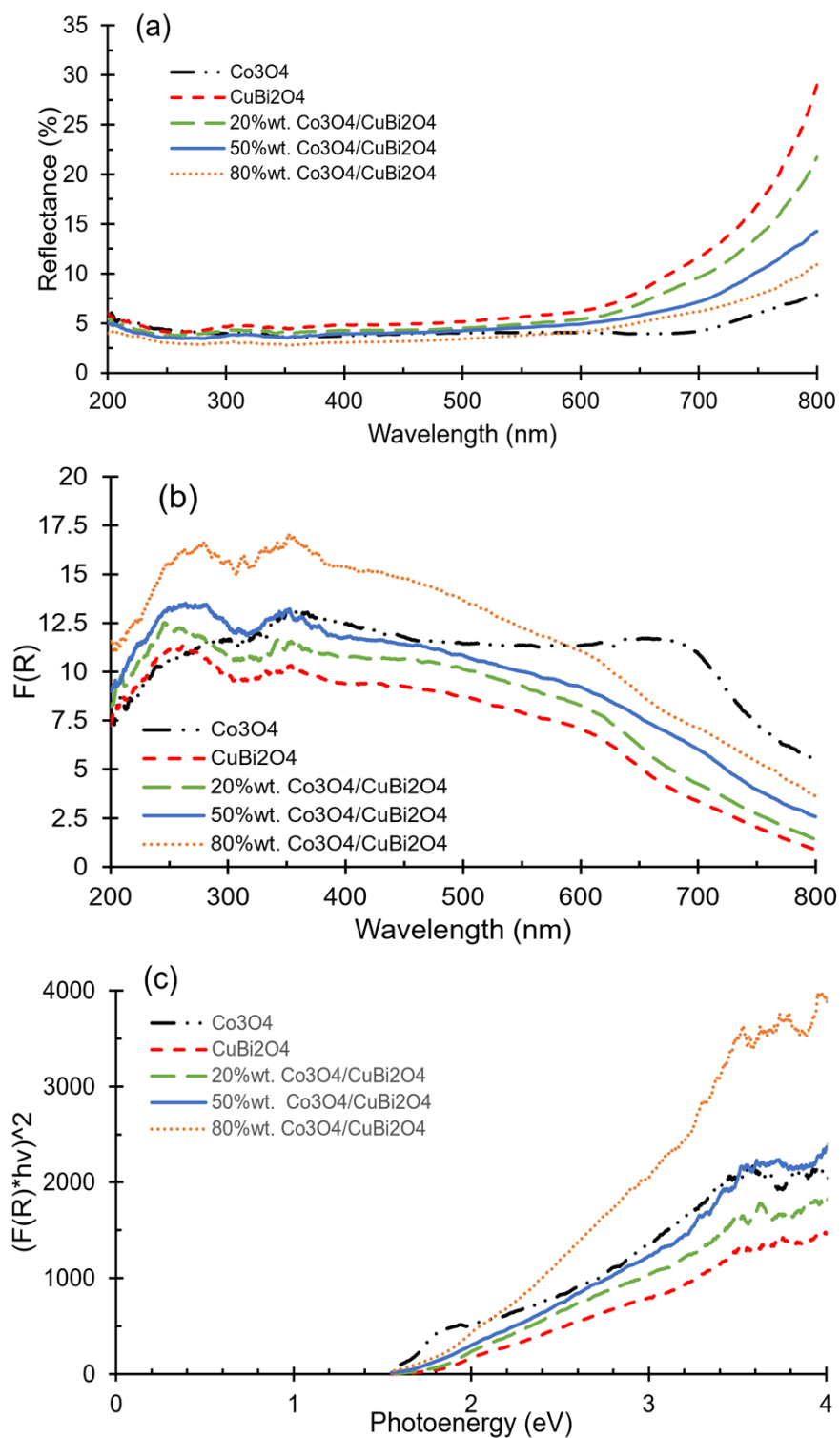


Figure 32 (a) UV-vis diffuse reflectance spectra (b) Kubelka-Munk absorbance spectra, and (c) band gap estimation according to Tauc's model

Table 6 Optical properties in term of absorption edge and band gap

Sample	Absorption edge (nm)	Band gap (eV)
Co ₃ O ₄	620	2.0
CuBi ₂ O ₄	459	2.7
20% wt. Co ₃ O ₄ /CuBi ₂ O ₄	459	2.7
50% wt. Co ₃ O ₄ /CuBi ₂ O ₄	496	2.5
80% wt. Co ₃ O ₄ /CuBi ₂ O ₄	443	2.8

4.7 Photocatalytic activity test

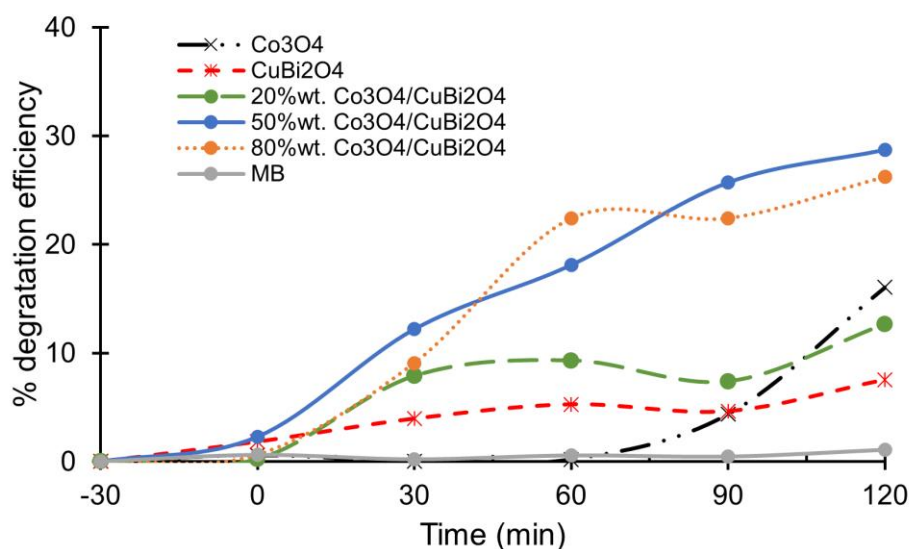
The photocatalytic degradation of MB dyes was investigated in the presence of Co₃O₄, CuBi₂O₄, and Co₃O₄/CuBi₂O₄ composite. The percentage of MB photocatalytic degradation was investigated as a function of visible light irradiation, as shown in **Figure 33**.

Before light irradiation, the mixed suspension was magnetically stirred in the dark for 30 min to reach complete adsorption/desorption equilibrium. It was found that both of Co₃O₄ and CuBi₂O₄ presented only ~1% of MB dark adsorption and only 3% of MB was obtained for all Co₃O₄/CuBi₂O₄ composites samples. The adsorption capacity of adsorbed MB molecules is proportional to the specific surface area values reported by BET study. Additionally, without photocatalyst (MB blank), no photolysis was observed, indicating that the removal of MB only occurred through photocatalytic process.

Under the visible irradiation, pure Co₃O₄ degraded ~ 16% of MB after 120 min under visible irradiation, while CuBi₂O₄ degraded about 7.5% of MB at the same condition. All Co₃O₄/CuBi₂O₄ composite shows better photocatalytic performance than pure Co₃O₄ and CuBi₂O₄ by the photoactivity decreases in the following order: 50% > 80% > 20% wt.Co₃O₄/CuBi₂O₄, as listed in **Table 7**. The highest photoactivity under visible light was observed for 50% wt.Co₃O₄/ CuBi₂O₄ composite. This better photocatalytic activity can be explained by electron transfer through Co₃O₄/CuBi₂O₄ heterojunction working under visible light. Further explanations of electron transport through heterojunction were discussed later in **Figure 34**.

Table 7 Comparison of photocatalytic activity

Sample	Photocatalytic activity	Apparent rate constant (k)
	(%)	min ⁻¹
Co ₃ O ₄	16%	0.0011
CuBi ₂ O ₄	7.5%	0.0008
20% wt. Co ₃ O ₄ /CuBi ₂ O ₄	12%	0.0012
50% wt. Co ₃ O ₄ /CuBi ₂ O ₄	28%	0.0030
80% wt. Co ₃ O ₄ /CuBi ₂ O ₄	26%	0.0028

**Figure 33 Photocatalytic degradation of MB over different photocatalysts in visible light**

In general, the kinetics of photocatalytic reactions of most organic compounds are described by pseudo first-order decay kinetics rationalized in terms of the Langmuir–Hinshelwood model (51-53). In this study, the first approach takes photochemical reaction in the solution into account in addition to the photocatalytic photodegradation reaction on the catalyst. It can be assumed that the photocatalytic degradation of MB over CuBi₂O₄ photocatalyst is a pseudo first-order reaction. Pseudo first-order kinetic equation has the following form:

$$-\ln C_t/C_o = kt$$

The apparent rate constant (k , min^{-1}) can be determined by the slope of the linear line as presented in **Figure 34**.

The calculated value of the pseudo-first-order rate constant is presents in Table 7 (51-52). The apparent reaction rate constant (k) of the 50% wt. $\text{Co}_3\text{O}_4/\text{CuBi}_2\text{O}_4$ is 0.003 min^{-1} , which is almost 3 times greater than that of pure Co_3O_4 , and around 4 time compared to pure CuBi_2O_4 .

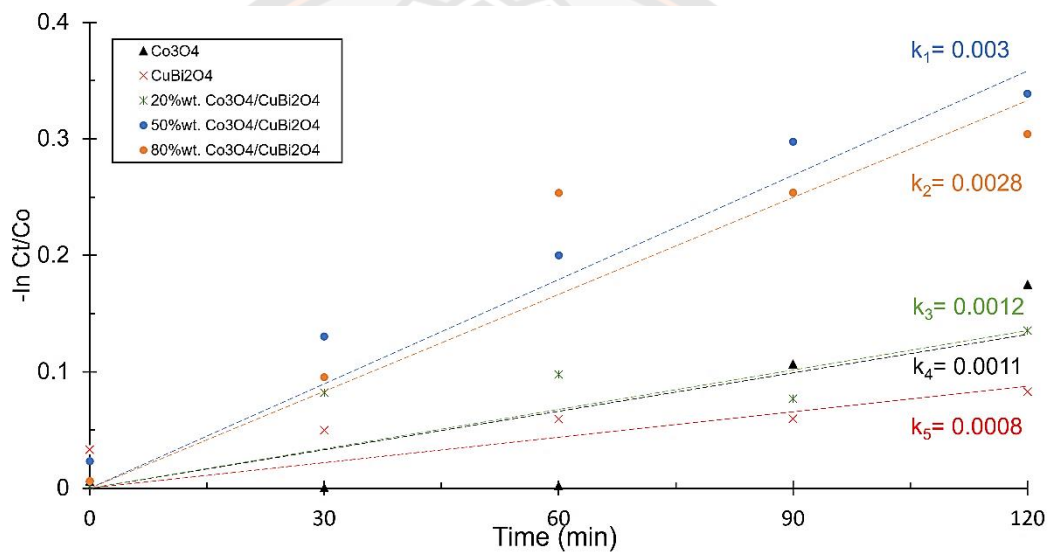


Figure 34 The apparent reaction rate constants

When Co_3O_4 content was added up to 80% wt, the degradation rate does not rise, rather being reduced due to too much amount of Co_3O_4 themselves can become the recombination center that suppresses the carrier separation.

To explain the proposed photocatalytic mechanism, the valance band (VB) and conduction band (CB) edge position can be calculated by the following equation using the electronegativity (54) and experimental band gap value.

$$E_{\text{CB}} = E_{\text{VB}} - E_g$$

$$E_{\text{VB}} = \chi - 4.5 + 0.5E_g$$

where χ is the absolute electronegativity (5.90 eV for Co_3O_4 and 4.59 eV for CuBi_2O_4) (55-56), E_g is the estimated band gap energy of Co_3O_4 and CuBi_2O_4 from this study (2.0 and 2.7 eV), E_{VB} and E_{CB} are the valence band edge and conduction band edge, respectively. The calculated values of band edges of Co_3O_4 and CuBi_2O_4 are listed in **Table 8**.

Table 8 The CB and the VB positions of Co_3O_4 and CuBi_2O_4

Sample	χ	E_g (eV)	E_{CB} (eV)	E_{VB} (eV)
Co_3O_4	5.90	2.0	0.40	2.40
CuBi_2O_4	4.59	2.7	-1.26	1.44

In **Figure 35**, proposes a possible photodegradation mechanism and band structure of the $\text{Co}_3\text{O}_4/\text{CuBi}_2\text{O}_4$ heterojunction. The matching band potentials between two semiconductors are recognized to be the driving factor for charge transfer. According to the VB and CB potentials of CuBi_2O_4 (1.44 and -1.26 eV, respectively) and those of Co_3O_4 (2.40 and 0.40 eV, respectively), the prepared composites provided matching energy band structures as type II band alignments (staggered band gap).

The photocatalytic mechanism of organic compounds in the presence of photocatalyst can be divided into three steps:

- (i) adsorption of organic pollutant on the surface of photocatalyst,
- (ii) photodegradation of the adsorbed organic compounds on the surface
- (iii) desorption of products of photocatalytic degradation from this surface

Under visible light illumination, both Co_3O_4 and CuBi_2O_4 are photoexcited to generate electrons and holes. These photogenerated electrons on the CB of CuBi_2O_4 migrates from CuBi_2O_4 with a higher CB position to Co_3O_4 , which has a lower CB position, and could effectively react with O_2 adsorbed on the surface of CuBi_2O_4 to produce superoxide radicals ($\text{O}_2^{\cdot-}$). Then, the superoxide radicals are turned into hydroxyl radicals ($\cdot\text{OH}$). After that, hydroxyl radicals could finally react with MB dye molecule adsorption on the photocatalyst surface. The hydroxyl radicals as active species can directly with MB dye molecules on the photocatalyst surface to decolorize the MB dye, and the small molecules can be mineralized to form CO_2 and H_2O (57).

For the oxidation reaction at VB, since the VB position (1.44 eV) of CuBi_2O_4 is less than the VB position of Co_3O_4 (2.40 eV), thus the photogenerated holes in the VB of Co_3O_4 will move to the VB of CuBi_2O_4 to react with surface bound H_2O to produce hydroxyl radicals.

In this case, Co_3O_4 as an electron sink and CuBi_2O_4 acts as a hole sink. Therefore, an effective charge separation of electron and hole could be achieved, resulting in enhancement of photocatalytic activity in composite sample.

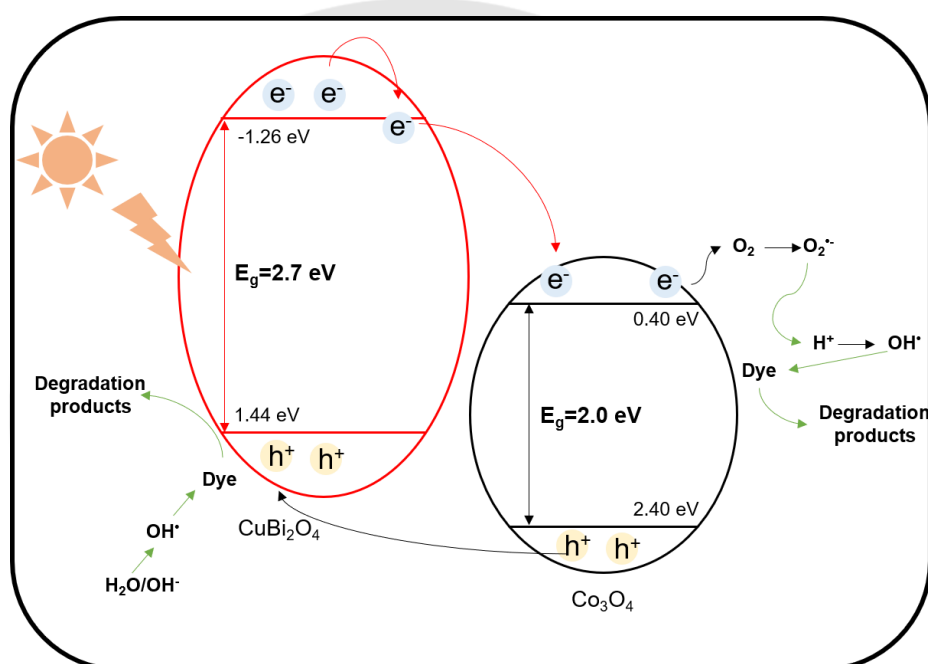


Figure 35 Schematic of photocatalytic reaction over the $\text{Co}_3\text{O}_4/\text{CuBi}_2\text{O}_4$ composite

To confirm the presence of the hydroxyl radicals (OH^\bullet) generated in the catalytic process, the terephthalic acid (TA) non-fluorescent substance reacts with OH^\bullet to yield the fluorescent product of 2-hydroxyterephthalic acid (TAOH) (58,59). The fluorescence emission intensity of TAOH at 425 nm can be related to the amount of the OH^\bullet generation. **In Figure 36** shows time-dependent fluorescence emission TAOH solutions generated by $\text{Co}_3\text{O}_4/\text{CuBi}_2\text{O}_4$ under visible-light irradiation. The PL intensities of TAOH at 425 nm steadily increased with the increased irradiation time

from 60 to 120 min, revealing that more and more OH[•] were produced with increasing irradiation time.

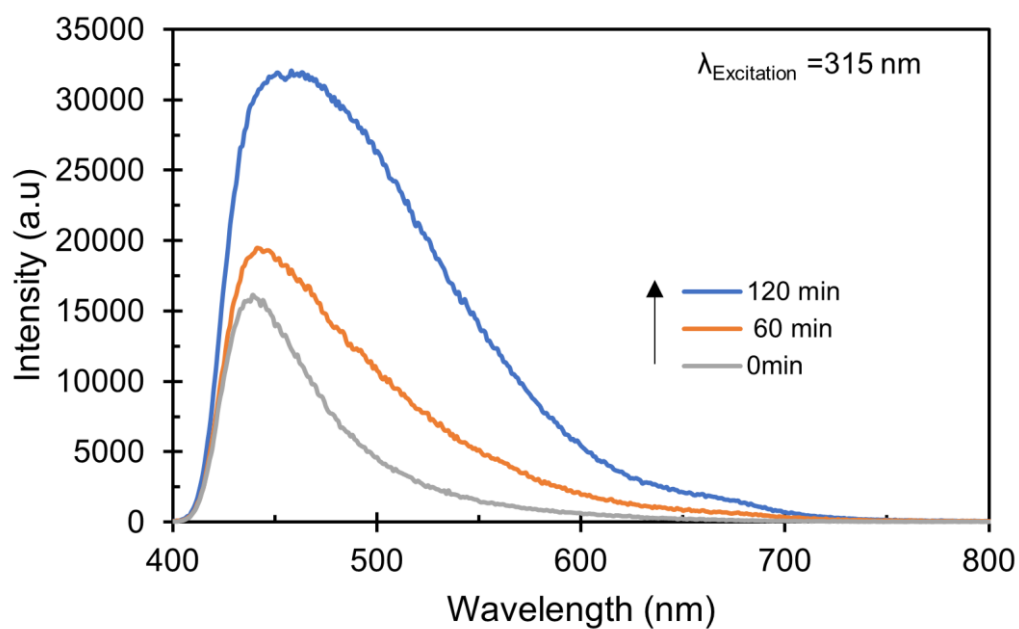


Figure 36 Fluorescence spectra of TAOH solutions generated by $\text{Co}_3\text{O}_4/\text{CuBi}_2\text{O}_4$ composite

CHAPTER V

CONCLUSIONS

In summary, this study successfully prepared spinel Co_3O_4 , tetragonal CuBi_2O_4 , and $\text{Co}_3\text{O}_4/\text{CuBi}_2\text{O}_4$ composites with different contents of Co_3O_4 (20, 50, 80% wt.). Among the various composites, 50 % wt. $\text{Co}_3\text{O}_4/\text{CuBi}_2\text{O}_4$ showed the highest photocatalytic activity after 120 min h of visible-light irradiation. The enhancement of composite photocatalysts can be attributed to:

- The formation of heterojunctions of Co_3O_4 and CuBi_2O_4 resulted in the efficient separation of electron–hole pairs to retard electron–hole recombination.
- An increase in the specific surface area of the mixed phase of spherical-shaped Co_3O_4 and plate-like CuBi_2O_4 , which provides more active sites for the adsorption of the MB dye molecules on the photocatalyst surface for further degradation under light-irradiation.

Based on the modification method, the experimental results reported in this study may be useful for the development of other photocatalysts. Furthermore, this work provided an idea for modification strategies-based composite photocatalysts to design optimized composite systems with better photocatalytic performance for future environmental applications.



REFERENCES

REFERENCES

1. Choi K-I, Kim H-R, Kim K-M, Liu D, Cao G, Lee J-H. C₂H₅OH sensing characteristics of various Co₃O₄ nanostructures prepared by solvothermal reaction. *Sensors and Actuators B: Chemical*. 2010;146(1):183-9.
2. Ahmed SN, Haider W. Heterogeneous photocatalysis and its potential applications in water and wastewater treatment: a review. *Nanotechnology*. 2018;29(34):342001.
3. Guerreiro LF, Rodrigues CSD, Duda RM, de Oliveira RA, Boaventura RAR, Madeira LM. Treatment of sugarcane vinasse by combination of coagulation/flocculation and Fenton's oxidation. *J Environ Manage*. 2016;181:237-48.
4. Wang HW, Li XY, Hao ZP, Sun YJ, Wang YN, Li WH, et al. Transformation of dissolved organic matter in concentrated leachate from nanofiltration during ozone-based oxidation processes (O₃, O₃/H₂O₂ and O₃/UV). *J Environ Manage*. 2017;191:244-51.
5. Speidel A, Mitchell-Smith J, Bisterov I, Clare AT. The importance of microstructure in electrochemical jet processing. *Journal of Materials Processing Technology*. 2018;262:459-70.
6. Yana Y, KS, YS, YZ, JG, LD, et al. Adsorption and Agglomeration Characteristics of Ash Particles after Reducing Flue Gas Temperature below the Acid Dew Point. 9th International Conference on Applied Energy; 21-24 August 2017. 2017.

7. Sable SS, Shah KJ, Chiang P-C, Lo S-L. Catalytic oxidative degradation of phenol using iron oxide promoted sulfonated-ZrO₂ by Advanced Oxidation Processes (AOPs). *Journal of the Taiwan Institute of Chemical Engineers*. 2018;91:434-40.
8. Liu Y, Lin Y, Liu Z, Tang J, Chen L, Liu X, et al. Self-generating CoFe₂O₄ as electric channel in Z-scheme CoO(111)/CoFe₂O₄/Fe₂O₃ photocatalyst for synchronous photocatalytic degradation and hydrogen production. *Materials Science in Semiconductor Processing*. 2022;140.
9. Lakra R, Kumar R, Nath Thatoi D, Kumar Sahoo P, Soam A. Synthesis and characterization of cobalt oxide (Co₃O₄) nanoparticles. *Materials Today: Proceedings*. 2021;41:269-71.
10. Zhang H, Tian W, Zhou L, Sun H, Tade M, Wang S. Monodisperse Co₃O₄ quantum dots on porous carbon nitride nanosheets for enhanced visible-light-driven water oxidation. *Applied Catalysis B: Environmental*. 2018;223:2-9.
11. Shao J, Zhou H, Zhu M, Feng J, Yuan A. Facile synthesis of metal-organic framework-derived Co₃O₄ with different morphologies coated graphene foam as integrated anodes for lithium-ion batteries. *Journal of Alloys and Compounds*. 2018;768:1049-57.
12. Zhang B, Cheng M, Liu G, Gao Y, Zhao L, Li S, et al. Room temperature NO₂ gas sensor based on porous Co₃O₄ slices/reduced graphene oxide hybrid. *Sensors and Actuators B: Chemical*. 2018;263:387-99.
13. Xu D, Xia T, Fan W, Bai H, Ding J, Mao B, et al. MOF-derived Co₃O₄ thin film decorated BiVO₄ for enhancement of photoelectrochemical water splitting. *Applied Surface Science*. 2019;491:497-504.

14. Xie C, Wang Y, Zhang Z-X, Wang D, Luo L-B. Graphene/Semiconductor Hybrid Heterostructures for Optoelectronic Device Applications. *Nano Today*. 2018;19:41-83.
15. Itteboina R, Sau TK. Sol-gel synthesis and characterizations of morphology-controlled Co_3O_4 particles. *Materials Today: Proceedings*. 2019;9:458-67.
16. Oskar G. CHAPTER I – Application of dyes by dyeing. *The chemistry of synthetic dyes*. 1971;4 : 1-17.
17. Karl N. CHAPTER II - Application of dyes in textile printing. *The chemistry of synthetic dyes* . 1971;4:75-102.
18. Chaudhry A, Bashir F, Adil SF, Saif S, Shaik MR, Hatshan MR, et al. Ascorbic acid-mediated Fe/Cu nanoparticles and their application for removal of COD and phenols from industrial wastewater. *Journal of King Saud University - Science*. 2022;34(4).
19. Muhammad MT, Khan MN. Eco-friendly, biodegradable natural surfactant (*Acacia Concinna*): An alternative to the synthetic surfactants. *Journal of Cleaner Production*. 2018;188:678-85.
20. Gu M, Yin Q, Wang Z, He K, Wu G. Color and nitrogen removal from synthetic dye wastewater in an integrated mesophilic hydrolysis/acidification and multiple anoxic/aerobic process. *Chemosphere*. 2018;212:881-9.
21. Rayaroth MP, Aravindakumar CT, Shah NS, Boczkaj G. Advanced oxidation processes (AOPs) based wastewater treatment - unexpected nitration side reactions - a serious environmental issue: A review. *Chemical Engineering Journal*. 2022;430.

22. Kubo D, Kawase Y. Hydroxyl radical generation in electro-Fenton process with in situ electro-chemical production of Fenton reagents by gas-diffusion-electrode cathode and sacrificial iron anode. *Journal of Cleaner Production*. 2018;203:685-95.
23. Gabe Y, Miyaji A, Kohno M, Hachiya A, Moriwaki S, Baba T. Substantial evidence for the rhododendrol-induced generation of hydroxyl radicals that causes melanocyte cytotoxicity and induces chemical leukoderma. *J Dermatol Sci*. 2018;91(3):311-6.
24. Wang L, Wu R, Xu C. Atmospheric oxidation mechanism of benzene. Fates of alkoxy radical intermediates and revised mechanism. *J Phys Chem A*. 2013;117(51):14163-8.
25. Grabowska E, Marchelek M, Paszkiewicz-Gawron M, Zaleska-Medynska A. Metal oxide photocatalysts. *Metal Oxide-Based Photocatalysis* 2018. p. 51-209.
26. Antonopoulou M, Kosma C, Albanis T, Konstantinou I. An overview of homogeneous and heterogeneous photocatalysis applications for the removal of pharmaceutical compounds from real or synthetic hospital wastewaters under lab or pilot scale. *Sci Total Environ*. 2021;765:144163.
27. Rosa JM, Fileti AMF, Tambourgi EB, Santana JCC. Dyeing of cotton with reactive dyestuffs: the continuous reuse of textile wastewater effluent treated by Ultraviolet / Hydrogen peroxide homogeneous photocatalysis. *Journal of Cleaner Production*. 2015;90:60-5.
28. Andreozzi R, Canterino M, Marotta R. Fe(III) homogeneous photocatalysis for the removal of 1,2-dichlorobenzene in aqueous solution by means UV lamp and solar light. *Water Res*. 2006;40(20):3785-92.

29. Yetim AF, Kovacı H, Kasapoğlu AE, Bozkurt YB, Çelik A. Influences of Ti, Al and V metal doping on the structural, mechanical and tribological properties of DLC films. *Diamond and Related Materials*. 2021;120.
30. Bouferra R, Marín G, Amhil S, Wasim SM, Essaleh L. Low temperature electrical impedance spectroscopy characterization of n type CuInSe₂ semiconductor compound. *Physica B: Condensed Matter*. 2019;565:14-7.
31. Tuerdi A, Abdukayum A, Chen P. Synthesis of composite photocatalyst based on the ordered mesoporous carbon-CuO with high photocatalytic activity. *Materials Letters*. 2017;209:235-9.
32. Basanta Roul, Mahesh Kumar, Mohana K Rajpalke , Thirumaleshwara N Bhat, Krupanidhi aSB. Binary group III-nitride based heterostructures: band offsets and transport properties. *Journal of Physics D: Applied Physics*. 2015;48:423001.
33. Gonçalves NPF, Paganini MC, Armillotta P, Cerrato E, Calza P. The effect of cobalt doping on the efficiency of semiconductor oxides in the photocatalytic water remediation. *Journal of Environmental Chemical Engineering*. 2019;7(6).
34. Akhlaghi N, Najafpour-Darzi G, Younesi H. Facile and green synthesis of cobalt oxide nanoparticles using ethanolic extract of *Trigonella foenumgraceum* (Fenugreek) leaves. *Advanced Powder Technology*. 2020;31(8):3562-9.
35. Su Y, Liu H, Li C, Liu J, Song Y, Wang F. Hydrothermal-assisted defect engineering in spinel Co₃O₄ nanostructures as bifunctional catalysts for oxygen electrode. *Journal of Alloys and Compounds*. 2019;799:160-8.
36. Sean P. B, Fatwa F. A, Peter B, Abdelkrim C, Dennis F, Roel v. d. K. Comprehensive Evaluation of CuBi₂O₄ as a Photocathode Material for

Photoelectrochemical Water Splitting. *Chemistry of Materials*. 2019; 28, 12: 4231–4242.

37. Freddy E. O, Nelson Y. D, Amalia P, Zhenni Y, Kelvin H. L.

Z, Nora H. de L, Emiel J. M. H, Jan P. H. Electronic Structure and Interface Energetics of CuBi_2O_4 Photoelectrodes. *The Journal of Physical Chemistry C*. 2020;124:22416-22425.

38. Ranjith R, Renganathan V, Chen S-M, Selvan NS, Rajam PS. Green synthesis of reduced graphene oxide supported $\text{TiO}_2/\text{Co}_3\text{O}_4$ nanocomposite for photocatalytic degradation of methylene blue and crystal violet. *Ceramics International*. 2019;45(10):12926-33.

39. Khan F. Statistical applications for photocatalytic dye degradation and sorption models study assess by Co_3O_4 nanoadsorbent. *Materials Today Chemistry*. 2020;17.

40. Keerthana SP, Yuvakkumar R, Kumar PS, Ravi G, Vo DN, Velauthapillai D. Influence of tin (Sn) doping on Co_3O_4 for enhanced photocatalytic dye degradation. *Chemosphere*. 2021;277:130325.

41. Chinnathambi A, Nasif O, Alharbi SA, Khan SS. Enhanced optoelectronic properties of multifunctional MnFe_2O_4 nanorods decorated Co_3O_4 nanoheterostructure: Photocatalytic activity and antibacterial behavior. *Materials Science in Semiconductor Processing*. 2021;134.

42. Yahong Xie, Yun Zhang , Guihua Yang , Chunhui Liu , Jide Wang. Hydrothermal synthesis of CuBi_2O_4 nanosheets and their photocatalytic behavior under visible light irradiation. *Materials Letters*. 2013;107:291-294.

43. Abdelkader E, Nadjia L, Ahmed B. Preparation and characterization of novel $\text{CuBi}_2\text{O}_4/\text{SnO}_2$ p–n heterojunction with enhanced photocatalytic performance under UVA light irradiation. *Journal of King Saud University - Science*. 2015;27(1):76-91.
44. Ramezanalizadeh H, Rafiee E. Design, fabrication, electro- and photoelectrochemical investigations of novel $\text{CoTiO}_3/\text{CuBi}_2\text{O}_4$ heterojunction semiconductor: An efficient photocatalyst for the degradation of DR16 dye. *Materials Science in Semiconductor Processing*. 2020;113.
45. Sabri M, Habibi-Yangjeh A, Ghosh S. Novel $\text{ZnO}/\text{CuBi}_2\text{O}_4$ heterostructures for persulfate-assisted photocatalytic degradation of dye contaminants under visible light. *Journal of Photochemistry and Photobiology A: Chemistry*. 2020;391.
46. Berglund SP, Abdi FF, Bogdanoff P, Chemseddine A, Friedrich D, van de Krol R. Comprehensive Evaluation of CuBi_2O_4 as a Photocathode Material for Photoelectrochemical Water Splitting. *Chemistry of Materials*. 2016;28(12):4231-42.
47. Gong L, Chng XYE, Du Y, Xi S, Yeo BS. Enhanced Catalysis of the Electrochemical Oxygen Evolution Reaction by Iron(III) Ions Adsorbed on Amorphous Cobalt Oxide. *ACS Catalysis*. 2017;8(2):807-14.
48. Ambroz F, Macdonald TJ, Martis V, Parkin IP. Evaluation of the BET Theory for the Characterization of Meso and Microporous MOFs. *Small Methods*. 2018;2(11).
49. Lahmar H, Benamira M, Akika FZ, Trari M. Reduction of chromium (VI) on the hetero-system $\text{CuBi}_2\text{O}_4/\text{TiO}_2$ under solar light. *Journal of Physics and Chemistry of Solids*. 2017;110:254-9.

50. Dong F, Xiao X, Jiang G, Zhang Y, Cui W, Ma J. Surface oxygen-vacancy induced photocatalytic activity of La(OH)₃ nanorods prepared by a fast and scalable method. *Phys Chem Chem Phys*. 2015;17(24):16058-66.
51. Pal B, Hata T, Goto K, Nogami G. Photocatalytic degradation of o-cresol sensitized by iron–titania binary photocatalysts. *J. Mol. Catal. A Chem*. 2001;169:147–155.
52. Botelho G, Andrés J, Gracia L, Matos L.S, Longo E. Photoluminescence and Photocatalytic Properties of Ag₃ PO₄ Microcrystals: An Experimental and Theoretical Investigation. *Chem Plus Chem*. 2015;81:202–212.
53. Beata S, Piotr S, Dariusz W, Marianna C, and Laura F. Kinetics and Mechanism of Aniline and Chloroanilines Degradation Photocatalyzed by Halloysite-TiO₂ and Halloysite-Fe₂O₃ Nanocomposites. *Catalysts*. 2021; 11(12): 1548.
54. Denis A. K, Binghong H, Yang Y, Reshma R. R, Jonathan H, Yuriy, Yang S. Tuning Redox Transitions via Inductive Effect in Metal Oxides and Complexes, and Implications in Oxygen Electrocatalysis. Elsevier Inc. 2017; 2: 225–244
55. Soleimani F, Salehi M, Gholizadeh A. Comparison of visible light photocatalytic degradation of different pollutants by (Zn, Mg)_xCu_{1-x}Bi₂O₄ nanoparticles. *Ceramics International*. 2019;45(7):8926-39.
56. Z S Chen AKYWTCCACKHYEC. FipoQ/FBXO₃³, a Cullin-1-based ubiquitin ligase complex component modulates ubiquitination and solubility of polyglutamine disease protein. *J Neurochem*. 2019;149(6):781-98.

57. Wu Z, Xue Y, Zhang Y, Li J, Chen T. SnS₂ nanosheet-based microstructures with high adsorption capabilities and visible light photocatalytic activities. RSC Advances. 2015;5(31):24640-8.
58. X. Li, B. Jie, H. Lin, Z. Deng, J. Qian, Y. Yang, X. Zhang, Application of sulfate radicals-based advanced oxidation technology in degradation of trace organic contaminants (TrOCs): Recent advances and prospects, J. Environ. Manage. 308 (2022) 114664(1–12).
59. V.S. Lin, M. Grandbois, K. McNeill, Fluorescent molecular probes for detection of one-electron oxidants photochemically generated by dissolved organic matter, Environ. Sci. Technol. 51 (2017) 9033–9041.

